RANS COMPUTATION OF PROPELLER TIP VORTEX FLOW FOR STEADY AND UNSTEADY CASES

MD. SHAFIUL AZAM MINTU

RANS Computation of Propeller Tip Vortex Flow for Steady and Unsteady Cases

by

©Md. Shafiul Azam Mintu

A thesis submitted to the
School of Graduate Studies
in partial fulfillment of the
requirements for the degree of
Master of Engineering

Faculty of Engineering and Applied Science
Memorial University of Newfoundland

July 2011

Abstract

CFD simulations were conducted for different marine propellers at steady and unsteady flow conditions using a commercial RANS solver ANSYS® CFX®. For steady simulation, a spiral-like domain aligned with the vortex core was generated with structured grids. The simulation was validated with the David Taylor Model Basin DTMB 5168 propeller model at open-water condition.

Various eddy viscosity turbulence models and Reynolds-stress models were employed in the computations. The effect of the turbulence modeling on the solution was investigated. The blade surface pressure and the propeller performance were also computed. The simulation data were compared with the experimental data.

The unsteady simulation was conducted for propeller at inclined flow condition. A single domain was generated with structured grids. A simulation technique for inclined flow condition was presented. The simulation was validated with the model test data of DTMB 4718 at design condition. A fully implicit coupled solver was used. A segregated solver with Incomplete Lower Upper (ILU) factorisation technique was employed in the simulation. Algebraic Multi-grid (MG) model was used to accelerate the convergence. Advection terms were descretised by high resolution scheme while the viscous terms were treated by employing central difference scheme. The transient terms were descretised with Second Order Backward Euler scheme. The Shear Stress Turbulence model was employed in the computation.

The effect of grid sensitivity and domain size were investigated. The periodic loadings on the pressure and suction sides of the blades were compared with the

experimental data. Reasonable agreement with the computed amplitude of the pressure variations was found. The predictions of the phase of the pressure variations were less favourable.

This work is the first attempt of the CFD simulation for unsteady propeller flow investigation using a spiral like computational grid. Further improvements and extensions of this work can be made. Suggestions are made regarding future work on the use of CFD simulations of propeller flow.

Acknowledgements

I would like to express my sincere appreciation to my thesis supervisor Dr. Wei Qiu. He gave me complete freedom to try ideas and assisted me throughout my graduate studies at Memorial.

I would like to express appreciation to my many colleagues at the Advanced Marine Hydrodynamics Laboratory for their sincere cooperation.

Special thanks to Bruce Quinton, a PhD student at Memorial for his sincere cooperation and help in using STePS2's cluster server. Thanks are extended to STePS2 for permitting me to use their cluster server. Without this the simulation experiment would run forever.

I gratefully acknowledge the support from the Natural Sciences and Engineering Research Council of Canada (NSERC), Defence Research and Development Canada-Atlantic (DRDC-Atlantic), Oceanic Consulting Corporation and Memorial University of Newfoundland (MUN).

Finally, I would like to thank my family for all their love and encouragement. They have sacrificed a lot due to my research abroad. Especially, I would like to give my special thanks to my wife Moon. She helped me to concentrate on completing this thesis and supported me mentally during the course of this work. Without her help and encouragement, this study would not have been completed.

Contents

List of Figures

List of Tables

Nomenclatures

BTE	Non-dimensional distance of the outlet boundary
c	Chord length of aerofoil
D	Diameter of propeller
FLE	Non-dimensional distance of the outlet boundary
h_{tot}	Total enthalpy
ILE	Indices of grid points on the leading edge
ITE	Indices of grid points on the trailing edge
i_T	Total rake of propeller
i_G	Generator line rake
i_T	Skew induced rake
$IMAX$	Number of grid points in the streamwise direction
$JMAX$	Number of grid points in the blade-to-blade direction
J	Advance coefficient
$KMAX$	Number of grid points on the boundary in the spanwise direction
$KTIPNUM$	Number of grid points on the blade surface in the spanwise direction
k	Turbulent kinetic energy
K_t	Propeller thrust coefficient, $T/(\rho n^2 D^4)$
K_q	Propeller torque coefficient, $Q/(\rho n^2 D^5)$
$L_{0.7R}$	Chord length at 0.7R
n	Rotational speed of propeller
Q	Total torque on propeller
r	Radial distance of propeller
r_H	Hub radius of propeller
R	Radius of propeller

$\boldsymbol{S}_M$	Momentum source
$\boldsymbol{S}_E$	Energy source
t	Aerofoil thickness
T	Total thrust on propeller
V_x	Axial velocities in the tangential direction across the tip vortex centre
V_t	Tangential velocities in the tangential direction across the tip vortex centre
V_r	Radial velocities in the tangential direction across the tip vortex centre
V_{Tot}	Total velocity
y^+	Non-dimensional wall distance
δ_k	Blade index angle
δ	Kronecker delta function
ρ	Density of water, $997kg/m^{-3}$
μ_{water}	Dynamic viscosity of water, $8.89 \times 10^{-4} kgm^{-1}s^{-1}$
θ	Skew angle of propeller blade
τ	Stress tensor
ϕ	Any variable of fluid properties
Γ	Diffusion coefficient
$\otimes$	Tensor product of two vectors
ω	Angular velocity
μ_t	Eddy viscosity or turbulent viscosity
ϵ	Turbulent dissipation rate
ω	Turbulent frequency

Chapter 1

Introduction

1.1 Background and Motivation

A marine propeller operating at the stern, within the wake of the ship, complicates the propeller hydrodynamics. The blade inflow varies significantly as the propeller rotates, producing unsteady forces. These forces result in additional unsteady loads on the shaft and cause vibration on the hull. When the loading on the blades increases, the propeller experiences another hydrodynamic phenomenon called cavitation, which degrades propeller performance, erodes blade surfaces, produces noise, and causes vibration on the ship hull. Apart from the vibration issues, the knowledge of the unsteady load distribution is essential for the blade fatigue analysis. It is also important for proper shaft and stern bearing design.

Additional complexity arises from the propeller operating with a shaft inclination. This shaft inclination generates unsteady loads on the blade surfaces and consequently creates vibration and cavitation. On the other hand, with the increasing demand for heavily loaded propellers, the occurrence of cavitation is unavoidable. Therefore, the accurate prediction of cavitation is important.

The cavitation phenomena can be revealed by experimental, analytical or numerical techniques. Experimental methods provide valuable insights into the cavitation physics in various predetermined conditions, but it is expensive to manufacture the models and they are vulnerable to slight flow condition changes inside cavitation tunnels (Rhee and Koutsavdis, 2003). They also seriously suffer from scale effects in viscous flow phenomena. Current analytical solutions can not predict periodic blade loads accurately. They underpredict the periodic propeller blade loads in inclined flow and give poor prediction of time average propeller blade loads at substantially off-design conditions (Jessup, 1982). On the other hand, numerical methods can provide insight into the local flow characteristics and are able to give sufficient information. The cost and time required for the computation are much lower than for model tests and are suitable for flow analysis.

The numerical methods based on potential theory are widely used in propeller flow analysis. The potential flow methods are based on the assumptions of inviscid fluid and irrotational motion. Using these methods, propeller performance at design conditions can be predicted quite accurately, for example, Kinnas and Hsin (1992), Gaggero et al. (2010). However, the off-design propeller flow phenomena, which are dominated by viscous effects, cannot be predicted accurately. Moreover, the potential flow methods are not able to predict the wake field with a sufficient level of accuracy. To take into account the highly viscous effect of the propeller flow field, it is proven that the numerical simulation based on the Reynolds-averaged Navier-Stokes (RANS) method is effective. The unsteady RANS method represents the state-of-the-art in computational prediction of the viscous flow around propellers (Chen and Stern, 1999).

The accurate simulation of unsteady propeller flows is a challenging task due to its complex physics and geometry. For example, general hub shapes can produce

a potential flow perturbation and will influence the inflow (Jessup, 1989). The boundary layer can develop on the blade surfaces and can cause large gradients of the velocity field (Qiu et al., 2010). The trailing edge flows may not maintain the constant pressure at the trailing edge. In the case of tip vortex flows, radial flows can separate at the tip through the adverse pressure gradients (Jessup, 1989). The complexity of the flow field and geometry require special techniques to generate suitable grids for the computational domain.

Another complexity for the propeller flow simulation arises from turbulence modeling. A screw propeller generates non-equilibrium regions in the boundary layer with adverse pressure gradients, and separation of flow may occur (Krasilnikov et al., 2009). It induces highly rotating flow and entails a tip vortex, which causes turbulence in the tip vortex region. The low Reynolds number (Re) flows occur at the near wall regions, while high Re flows develop at the far-field. Moreover, the propellers operating under off-design conditions develop strong flow separation on the blades. The simulation of propeller flow should take into account these flow phenomena. Limited studies were done to find the effects of turbulence modeling on the propeller tip vortex computations. The fluctuating flows should be treated with the appropriate turbulence models.

1.2 Objective of this Research

The objectives of this research work were to predict the viscous flows past propellers based on the RANS solutions. The commercial RANS solver ANSYS-CFX was used for this simulation. Both uniform and inclined inflow conditions were examined. A grid generation program *PropGGM*, developed by Qiu et al. (2003), was employed to generate a spiral like computational domain for the steady and unsteady simulations.

For the steady simulation, the propeller tip vortex flow was computed. The effect of turbulence modeling on the tip vortex computation was performed to investigate if the Reynolds stress model improves the tip vortex computations. For the unsteady case, the ANSYS CFX is used to predict the unsteady blade loads.

1.3 Organization of Thesis

A review of the past works is summarized in Chapter 2. Chapter 3 describes the process to develop the spiral like computational domain for the numerical simulation. Chapter 4 covers the governing equations describing the fluid flow and their descretisaton methods. Having explained the analysis process in Chapter 4, Chapter 5 describes the research findings. The last chapter gives the conclusions. Suggestions for future work are also presented.

Chapter 2

Review of Related Work

This chapter focuses on the literature review of work on steady and unsteady propeller blade flows. A brief summary of some of the major experimental and numerical work is presented. The scope of predicting propeller loads, for both steady and unsteady cases, using existing experimental and numerical methods are also discussed.

2.1 Steady Cases

2.1.1 Experimental Work

Advanced flow visualization and non-intrusive measurement techniques distinctly improve the experimental investigations of flow field studies on propellers. The first Laser Doppler Velocimeter (LDV) measurements of marine propeller flow were made by Min (1978) at MIT and further insight into the propeller wake was provided. The viscous wakes were identified. An extension of Min's study was carried out by Kobayashi (1981) to measure the viscous wake downstream of the propeller with some details. Cendese (1985) and Billet (1987) conducted LDV measurements about marine propellers with the inclusion of turbulent measurements. All of these experimental investigations have only identified the wake as complications in the flow with high turbulence, but detailed wake measurements had not been made. Chesnakas and

Jessup (1998) used LDV systems to obtain detailed velocity measurements of a propeller wake at downstream locations. Di Felice et al. (2004) demonstrated the capability of Particle Image Velocimetry (PIV) for identifying the flow structures in the wake of a propeller. In spite of the success in measurement of propeller flow features, the pressure field still remains unclear due to the limitations of measurement techniques. It is desirable to provide the detailed pressure field by numerical simulations.

2.1.2 Numerical Work

Panel methods have long been applied for the solution of propeller design and analysis of flow problems. Hess and Valarezo (1985) made the first attempt to analyse steady flow around a marine propeller using 3D Boundary Element Method. The classical Hess and Smith formulation had been used in this paper. Kerwin et al. (1987) also applied the panel method to investigate marine propellers performance. In recent years, numerous researchers have used RANS to simulate the rotating blade cases. For example, Abdel-Maksoud et al. (2004) analysed the effect of the hub cap shape on propeller performance using commercial RANS code, CFX-TASCflow. Abdel-Maksoud and Heinke (2002) predicted the velocity distribution in the gap region of a ducted propeller using the same code. Simonsen and Stern (2005) computed the hull-rudder-propeller interaction by coupling the RANS and potential codes. Rhee and Joshi (2003) presented the computations of marine propeller flow using the commercial RANS code, FLUENT. However, numerical studies on the tip vortex flow of open marine propellers are somehow limited except for some earlier studies, for example, Hsiao and Pauley (1999) and Chen and Stern (1998). Hsiao and Pauley (1999) applied a one-equation turbulence model on fine grids to compute the tip vortex flows. The tip vortex was better predicted at the location closer to the propeller while the wake was better predicted at the far field location. It was concluded that the eddy viscosity computed from the Baldwin-Barth one-equation

turbulence model might be too large within the tip vortex and led to an overly diffusive and dissipative tip vortex.

In this thesis, the steady-state tip vortex flow generated by a marine propeller was computed using the RANS solver ANSYS CFX. An investigation was done to show the effect of turbulence modeling on the vortex flow computation. Various eddy viscosity and Reynolds stress turbulence models were employed in the investigation.

2.2 Unsteady Cases

2.2.1 Experimental Work

The investigation on unsteady blade forces requires advanced experimental and numerical techniques. The total unsteady and time-average blade loads were evaluated by Boswell et al. (1976 and 1978) and Jessup et al. (1977). However, these results are unable to reveal significant information on the distribution of the periodic loadings over the blade and underpredict time-average blade loads at substantially off-design conditions. An experiment was undertaken by Jessup (1982) to obtain accurate and reliable measurements of the pressure distribution in uniform and inclined flow. He measured unsteady pressure distributions on the DTMB 4679 and DTMB 4718 models in oblique flow. Single blade forces for propeller DTMB 4661 in inclined flows of 10, 20, and 30 degrees were also reported by Boswell et al. (1981 and 1984). To acquire sufficient understanding of unsteady propeller hydrodynamics, Jessup (1990) did an experiment with the symmetric 3-bladed propeller DTMB 4119, which was operated behind harmonic wake screens with 3, 6, 9 and 12 cycles per revolution.

2.2.2 Numerical Work

Panel methods have been employed to compute steady and unsteady flows around propellers. Kerwin and Lee (1978) proposed a lifting surface method. Liu and Bose (1998) implemented inflow wake and hyperboloid panel algorithm to deal with the oblique flow for highly skewed propellers. Hsin (1990) and Gaggero (2010) solved the unsteady cavitating flow by a potential boundary element method. Politis (2004) applied the boundary element method to predict unsteady trailing vortex sheets emanating from each blade. However, the panel methods are limited to inviscid fluids only. When viscous flow becomes important, for example, for tip vortex predictions and leading and hub vortices predictions, the panel methods are unable to predict accurately. To overcome these limitations, viscous solvers must be used.

Most of the researchers have simulated the MIT FFX (Massachusetts Institute of Technology Flapping Foil Experiment) to reveal the physics of unsteady blade flow. For example, Rhee and Koutsavdis (2003) presented a two dimensional (2D) simulation of unsteady flow around the blade section embedded in a travelling wave field. In their work, an unstructured dynamic meshing technique was used. Paterson and Stern (1997) validated their time accurate solutions of the RANS equations by simulating the MIT FFX. Most marine propellers operate in a highly three dimensional and viscous inflow condition. In the case of a propeller with an inclined shaft, the propeller operates in a primary potential flow field, but the shaft inclination causes unsteady loads on the blades (Jessup, 1989). These practical configurations cause complex unsteady flow phenomena and need to be addressed.

Gaggero et al. (2010) used RANS solver StarCCM+ to investigate the oblique flow phenomenon on model propeller DTMB 4679 by using sliding mesh technique. This technique takes into account the relative motion of the propeller blade around an inclined axis inside the fixed domain in which the propeller inflow is generated.

This approach is known as mixing plane approach (Snchez-Caja et al., 2008). The advantage of the sliding mesh technique is that it allows for time accurate simulation. In their work, the whole domain was generated by unstructured grids. An implicit unsteady solution approach with algebraic multi-grid model were employed. Superior capabilities of the RANS solver were found over the potential solver in predicting the unsteady pressure distributions and forces at off-design conditions, although they also described the RANS solver as an immature tool for the solution of the steady and unsteady cavitating problem. Krasilnikov et al. (2009) also employed the sliding mesh technique in another CFD code, FLUENT. In their simulation, the widely used model propeller DTMB 4679 was simulated in two stages. At the first stage, the solution was done by using Moving Reference Frame (MRF). This solution was then used as initial conditions for time dependent simulation. Temporal discretization was done by first order accurate backward difference discretisation technique. The computational domain was generated by 2.86 million unstructured cells. From their computation, it was found that the RANS method predicted better in heavier loading conditions. Under lighter (J=1.078) loading, where the influence of viscosity is larger, the RANS calculation overpredicted the pressure on the suction side. The same case was also reported by Leras and Hally (2010), but for heavier loading (J=0.719). As explained by Leras and Hally (2010), it may be due to the cavitation at the tip which is ignored in the calculation. They also did a preliminary study with two model propellers, DTMB 4679 and DTMB 4718, to investigate inclined flow phenomenon using the commercial RANS solver ANSYS CFX. Two dimensional structured grids were used on the blades, and the remaining regions (hub and regions associated with the blade) were made by unstructured grids. The data for analysis were sampled on each blade over only one-third of a complete revolution and then added together to get the equivalent pressure on a single blade over a full revolution. Good agreements with the experimental data were found with the measured average pressures. The computed amplitudes of the pressure variations were also in

good agreement. However, the phase of the pressure variations were poorly predicted.

In this study, the numerical simulation was conducted to predict the flow around a propeller operating with a shaft inclination of 7.5°. The commercial RANS solver ANSYS CFX was used. A single domain was generated with structured grids. The simulation was validated with the model test data of DTMB 4718 at design condition. The periodic loadings on the face and back of the blade surface were computed and validated with the experimental data.

Chapter 3

Propeller Geometry and Grid Generation

The numerical solution of RANS equations requires discretization of the field of interest into a collection of points or elemental volumes. The efficiency of a RANS solver largely depends on the quality of grid. In this chapter, the geometry of propeller and the grid generation of the computational domain are discussed.

3.1 Propeller Geometry

The grid was generated by the program *PropGGM* (Qiu et al., 2003). The input of this program only takes the 3-Dimensional coordinates of the blade surface and does not include sectional pitch, chord length, pitch diameter ratio, skew and rake distributions. A Fortran program was then developed to generate the Cartesian coordinates of the blade by taking the basic propeller geometry. The mathematical formulation of the program is described below.

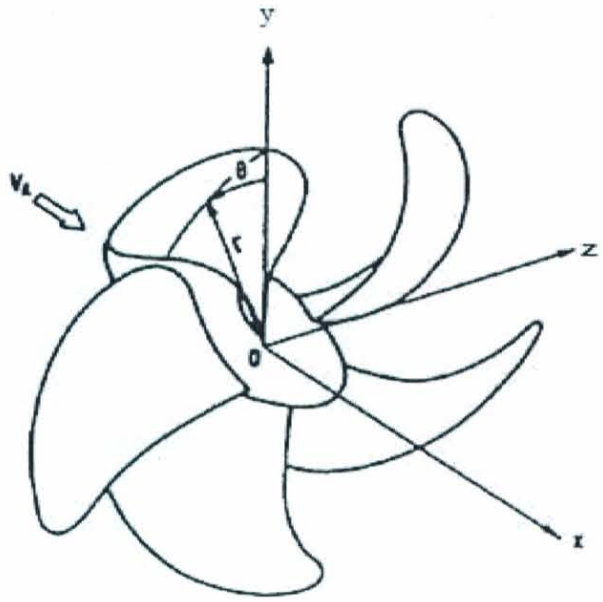

Figure 3-1: Coordinate system of propeller

3.1.1 Coordinate System

A cartesian coordinate system, $Oxyz$, fixed on the propeller is applied. The positive x-axis defined as downstream direction and y-axis located at any desired angular orientation relative to the key blade. The z-coordinate is determined by the right-handed system (Figure 3-1)

A cylindrical coordinate system is defined as follows. The angular coordinate θ is measured clockwise from the y-axis when viewed in the direction of positive x-axis. The radial and angular coordinates are given by

$$r = \sqrt{y^2 + z^2} \tag{3.1}$$

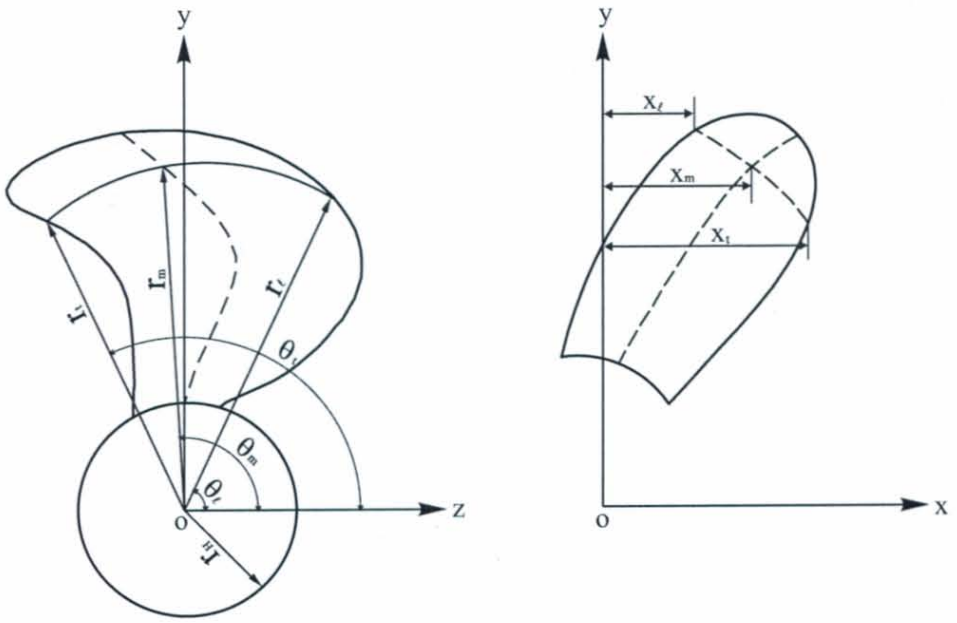

Figure 3-2: Cylindrical coordinate system

$$\theta = \tan^{-1}(y/z)$$

3.1.2 Blade Geometry

A projected view of a blade from upstream is shown in Figure 3-2. In the Figure, r_H is the hub radius, θ is the skew angle measured from the z-axis at radius r.

The skew angle, $\theta_m(r)$, is defined as the angular coordinate of the mid-chord line measured from the y-axis at radius r where the y-axis is along the propeller reference line. As shown in Figure 3-3 (Carlton, 1994), the rake of the propeller is divided into two components: generator line rake (i_G) and skew induced rake (i_s). The total rake of the section with respect to directrix (i_T) is given by

$$i_T(r) = i_G(r) + i_s(r)$$

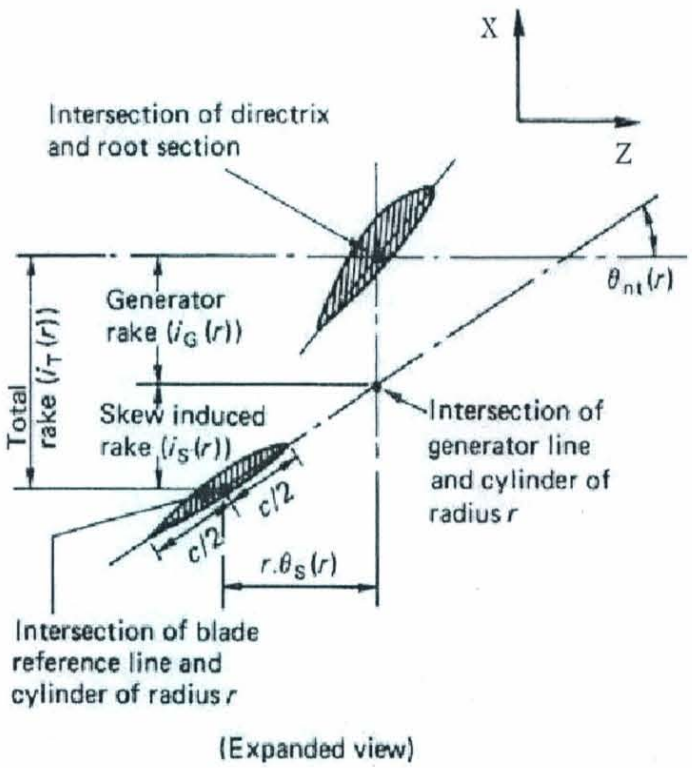

Figure 3-3: Definition of rake

The generator line rake, i_G, is simply the x-coordinate of the mid-chord line as shown in the Figure 3-2. The skew induced rake i_s, also measured in the x direction, is the component of helical distance around the cylinder from the mid-chord point of the section to the projection of the directrix when viewed normally to the yz-plane. The skew induced rake is given by as

$$i_s = r\theta_s \tan(\theta_{nt})$$

Where, θ_s section skew angle and θ_{nt} is the nose-tail pitch angle.

A blade index angle, δ_k, is defined to generalize the results to all blades other than

the key blade:

$$\delta_k = \frac{2\pi(k-1)}{K}, k = 1, 2, \cdots, K \tag{3.2}$$

where K is the number of blades and k is the index of any blade. The key blade is defined by the $k = 1$. The coordinates of a point on the pressure and suction surface of a section on the kth blade can be written as

$$x_{s,p} = x_m + c(s - \frac{1}{2}) \sin\phi - t_{s,p} \cos\phi \tag{3.3}$$

$$\theta_{s,p} = \theta_m + c(s - \frac{1}{2}) \frac{\cos\phi}{r} + t_{s,p} \frac{\sin\phi}{r} + \delta_k \tag{3.4}$$

$$y_{s,p} = -r \sin\theta_{s,p} \tag{3.5}$$

$$z_{s,p} = r \cos\theta_{s,p} \tag{3.6}$$

where the subscripts s and p denote the suction side and the pressure side surfaces, respectively; $t_{s,p}$ is the section surface and is measured in a cylindrical surface of radius r in a direction normal to the helical coordinate.

3.1.3 Blade Section Geometry

The National Advisory Committee for Aeronautics (NACA) in the USA, now known as NASA, developed a systematic series of aerofoil geometries. Some of these aerofoil shapes have been adopted for the design of marine propellers. Typical section used for ship propeller is NACA66 series with the mean line $a = 0.8$. The section geometry is given in the appendix. The mean line or camber line is the locus of the mid-points between the pressure side (upper) and suction side (lower) when measured perpendicular to the camber line, as shown in Figure 3-4 (Carlton, 1994). The two edge points of this camber line are known as leading and trailing edges of the aerofoil. The distance between these two points when measured along the

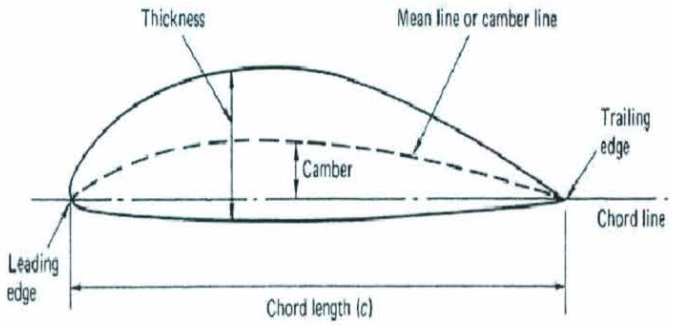

Figure 3-4: Definition of an aerofoil section

chord line is the chord length, c, of the section. The aerofoil thickness, t, is the distance between the upper and lower surfaces of the section, usually measured perpendicularly to the chord line.

The upper and lower surfaces are measured perpendicularly from the camber line. A point P_U on the upper surface and a point P_L on the lower surface of the aerofoil, as shown in Figure 3-5 (Carlton, 1994), are defined by

$$\begin{aligned} x_u &= x_c - y_t \sin\psi \\ y_u &= y_c + y_t \cos\psi \\ x_L &= x_c + y_t \sin\psi \\ y_L &= y_c - y_t \cos\psi \end{aligned} \tag{3.7}$$

where ψ, the slope of the camber line at the nondimensional chordal position, x_c, is defined as:

$$\psi = \tan^{-1}(\frac{y_c}{c}) \tag{3.8}$$

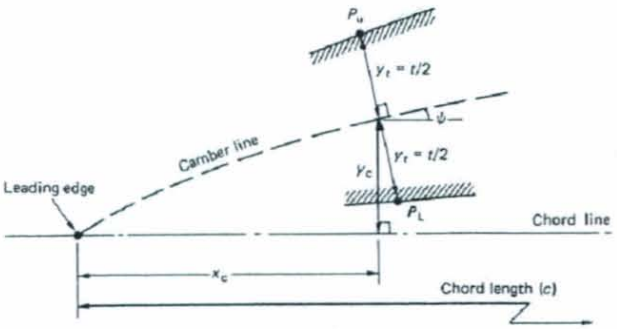

Figure 3-5: Aerofoil section definition

Since ψ is very small for marine propellers, Equations 3.7 can be simplified to

$$\begin{aligned} x_u &= x_c \\ y_u &= y_c + y_t \\ x_L &= x_c \\ y_L &= y_c - y_t \end{aligned} \tag{3.9}$$

where $y_t = t/2$ is the semi-thickness of the local section.

The leading edges are usually circular. But in the simulation the circular edge was replaced by a sharp edge for the ease of grid generation process.

3.1.4 Hub Geometry

Some geometry simplifications were made in the grid generation of the hub. The propeller blades were assumed to be mounted on an infinite constant-radius hub cylinder and therefore axial variation in hub radius was ignored. Root fillets for fixed-pitch propellers were also ignored.

3.2 Grid Generation Method

As stated earlier, the efficiency of RANS solver largely depends on the quality of the grid. For the computation of the propeller tip vortex flow, grid resolution within the tip vortex core has profound effect on the physical solutions (Hsiao and Pauley, 1999). To represent the physical solution with sufficient accuracy for a complex tip vortex flow, the following issues must be considered in the grid generation process (Qiu et al., 2003):

- **Grid Fineness:** A fine grid is necessary to adequately resolve the tip vortex. At least 15 grid points across the tip vortex core should be used to obtain a reliable near-field tip vortex for marine propellers (Hsiao and Pauley, 1999).
- **Grid Density:** The grid density on the propeller blade surface must be sufficient so that boundary layer effects can be well predicted.
- **Grid Smoothness:** Grids must be smooth throughout the computational domain.
- **Grid Orthogonality:** The grid orthogonality at the solid boundary is important if the zero normal pressure gradient approximation is applied.
- **Grid Efficiency:** The grid generator has to be computationally efficient for routine applications.

In this work, *PropGGM* was used for grid generation purpose. Detail description of the structure, functionalities, implementations and demonstration of this program is given by (Qiu et al., 2003). A brief description of the grid generation process is illustrated here.

3.2.1 Grid Generation Approach

The computational domain was created as one blade-to-blade passage with two periodic boundaries by following the inlet flow angle. One periodic boundary contains the suction side of a blade while the other contains the pressure side of the adjacent blade. This strategy resulted in a spiral-like computational domain. The advantage of this kind of computational domain is that the clustered grid can be easily aligned with the tip vortex and the flow across the periodic boundaries can be minimized (Hsiao and Pauley, 1999). The domain is enclosed by the inlet boundary upstream, the outlet boundary downstream, the inner boundary located on the hub surface and the outer boundary in the radial direction. The domain is shown in Figure 3-6. The grid generation was done by three steps:

- Step 1: Generation of the surface grid on the blade and hub surfaces.
- Step 2: Generation of a two-dimensional grid in the fluid domain between surfaces.
- Step 3: Smoothing the initial three-dimensional grid.

A brief discussion of each step is given below.

3.2.2 Grid Generation on Blade Surface

After the generation of blade surface coordinates, the surface grids were distributed on the blade surface. The panels generated from the original data shrinks to a point at the last radial station. This type of panels or grids are known as O-type grid and are not acceptable for a structured grid based RANS solver. To solve this issue, the data points from the original data were first increased. H-type grids were then generated from an O-type grids. Details of the H-type grid generation can be found in Qiu et al. (2003). Difference between H-type grids and O-type grids are shown in Figure 3-7.

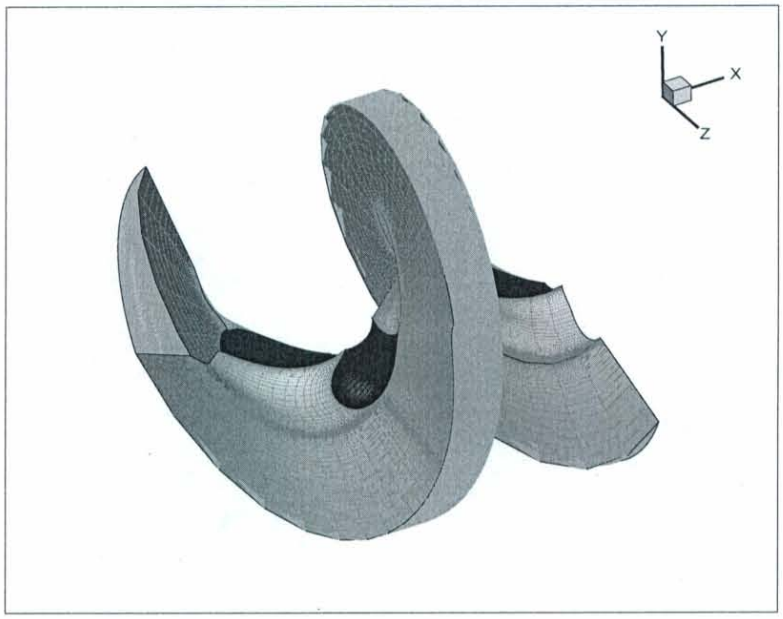

Figure 3-6: Spiral like computational domain

The distribution of H-type grid can be controlled by changing the number of grid points in the spanwise and chordwise directions as well as by the distribution functions. The distribution functions for grid points concentrated at two ends in the spanwise or chordwise direction are defined by

$$\phi(\xi) = \frac{(2\alpha+\beta)[(\beta+1)/(\beta-1)]^{(\xi-\alpha)/(1-\alpha)} + 2\alpha - \beta}{(2\alpha+1)\{1+[(\beta+1)/(\beta-1)]^{(\xi-\alpha)/(1-\alpha)}\}} \tag{3.10}$$

$$\psi(\zeta) = \frac{(2\alpha+\beta)[(\beta+1)/(\beta-1)]^{(\zeta-\alpha)/(1-\alpha)} + 2\alpha - \beta}{(2\alpha+1)\{1+[(\beta+1)/(\beta-1)]^{(\zeta-\alpha)/(1-\alpha)}\}} \tag{3.11}$$

where α and β are the gird distribution factor and stretching factor, respectively. When $\alpha = 0.5$, the grid will cluster evenly at both the tip and root regions in the spanwise direction or the leading and trailing edges in the chordwise direction.

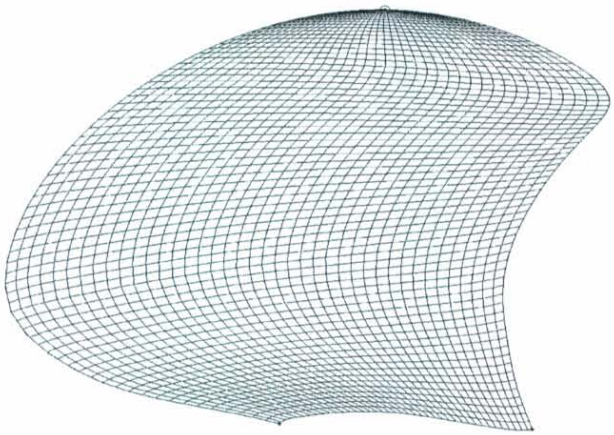

(a) O-type grid

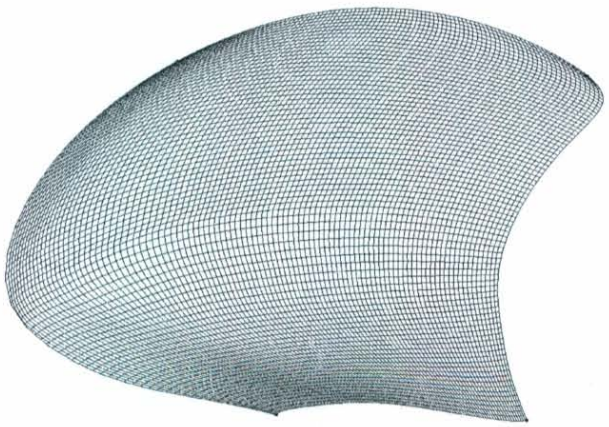

(b) H-type grid

Figure 3-7: Difference between H-type and O-type grid

The stretching factor, β, should be greater than one. The larger the value, the less concentration of grid points at the end edge will be achieved. In another words, the grid will be more uniformly distributed. The intermediate variables, ϕ and ψ, are defined on the unit intervals, ξ and ζ. In the program, $\xi = \frac{I-1}{N-1}$ and $\zeta = \frac{J-1}{M-1}$, where I or J is the order of the point in the chordwise direction or the spanwise direction, N or M is the total number of points in the chordwise direction or the spanwise direction. The location of a grid point on the surface can be controlled by adjusting the single valued function $\phi(\xi)$ in the chordwise direction or $\psi(\zeta)$ in the spanwise direction. The controlling functions for grid points concentrated at one end in the spanwise or chordwise direction are defined by

$$\phi(\xi) = \frac{(\beta+1) - (\beta-1)[(\beta+1)/(\beta-1)]^{1-\xi}}{[(\beta+1)/(\beta-1)]^{1-\xi} + 1} \tag{3.12}$$

$$\psi(\zeta) = \frac{(\beta+1) - (\beta-1)[(\beta+1)/(\beta-1)]^{1-\zeta}}{[(\beta+1)/(\beta-1)]^{1-\zeta} + 1} \tag{3.13}$$

For blade flow simulation, clustered grids are required at the tip and root regions as well as the leading and trailing edges of a blade surface. For this reason, the blade surface was subdivided into two regions in the spanwise direction. The first region was from $s = 0.0$ (root) to $s = 0.90$ where s is the non-dimensional arc length. The two-end grid concentration was applied in this region. The second region was from $s = 0.90$ to $s = 1.0$ (tip), where the one-end grid concentration was set. In the chordwise direction, the two regions were divided at $s = 0.45$. In the region close to the leading edge, two-end grid concentration was applied. In the other chordwise region, the one end grid concentration was used.

3.2.3 Grid Generation on Boundaries

To generate the spiral like boundary, the domain was divided into three regions as shown in the Figure 3-8. The first region is above the tip from the leading edge to

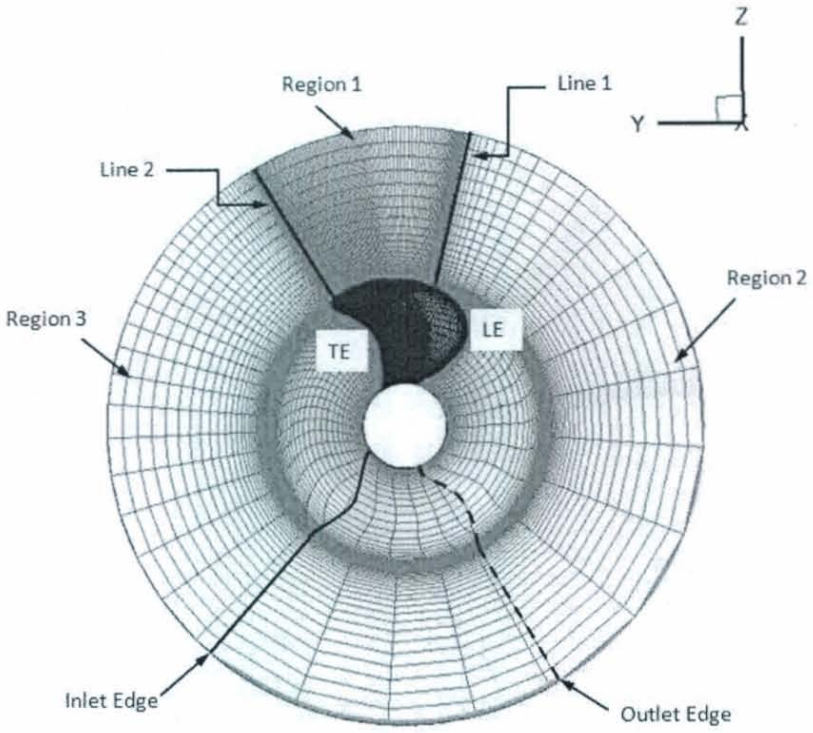

Figure 3-8: Grid generation on boundaries

the trailing edge, the region from the inlet boundary to the leading edge is the second region and the region from the trailing edge to the outlet boundary is Region 3.
To generate the grids in Region 1, the following equations were used (Qiu et al., 2003):

$$
\begin{aligned}
x(i,k) &= x(i, KTIPNUM) \\
r(i,k) &= r_{tip}(i) + \phi(k)\frac{r_{far} - r_{tip}(i)}{r_{tip-far}} \\
\theta(i,k) &= \theta(i, KTIPNUM) \\
y(i,k) &= r(i,k)\sin[\theta(i,k)]
\end{aligned}
\tag{3.14}
$$

$$z(i,k) = r(i,k)\cos[\theta(i,k)]$$

where, $i = ILE, ITE$; $k = KTIPNUM + 1, KMAX$. In the equations, ILE and ITE are the indices of grid points on the leading edge and the trailing edge, respectively, $KTIPNUM$ is the number of grid points on the blade surface in the spanwise direction, $KMAX$ is the total number of grid points on the boundary in the spanwise direction, $\phi(k)$ is the controlling function in the radial direction, $x(i, KTIPNUM)$, $\theta(i, KTIPNUM)$ and $r_{tip}(i)$ are the x, θ and r-coordinates at the tip, respectively.

To generate the grids in the Region 2, the following equations were used:

$$\begin{aligned}
x(i,k) &= x(ILE,k) - \frac{\phi(i)}{d_{LE}}[x(ILE,k) - x_{LE}] \\
r_\theta(k) &= [x(ILE,k) - x_{LE}]\frac{2\pi r^{'}(k)n}{U_\infty} \\
\theta(i,k) &= \theta(ILE,k) + \frac{\phi(i)}{d_{LE}}\frac{r_\theta(k)}{r^{'}(k)} \\
y(i,k) &= r(i,k)\sin[\theta(i,k)] \\
z(i,k) &= r(i,k)\cos[\theta(i,k)]
\end{aligned} \tag{3.15}$$

where, $i = ILE - 1, 1, -1$; $k = 1, KMAX$, $\phi(i)$ is the controlling function in the helix line direction, d_{LE} is the distance from the inlet boundary to the leading edge on the tip, x_{LE} is the x-coordinate of the inlet boundary, U_∞ is the inflow velocity, n is the RPS of the propeller, $r^{'}(k)$ is the radius of the grid on the line α, $x(ILE,k)$, $\theta(ILE,k)$ and $r(ILE,k)$ are the x, θ and r-coordinates on the leading edge, respectively.

For Region 3, the following equations were used:

$$
\begin{aligned}
x(i,k) &= x(ITE,k) + \frac{\phi(i)}{d_{TE}}[x_{TE} - x(ITE,k)] \\
r_\theta(k) &= [x_{TE} - x(ITE,k)]\frac{2\pi r^{'}(k)n}{U_\infty} \\
\theta(i,k) &= \theta(ITE,k) + \frac{\phi(i)}{d_{TE}}\frac{r_\theta(k)}{r^{'}(k)} \\
y(i,k) &= r(i,k)\sin[\theta(i,k)] \\
z(i,k) &= r(i,k)\cos[\theta(i,k)]
\end{aligned}
\tag{3.16}
$$

where, $i = ITE + 1, IMAX$; $k = 1, KMAX$, $\phi(i)$ is again the controlling function in the helix line direction, d_{TE} is the distance from the trailing edge to the outlet boundary on the tip, x_{TE} is the x-coordinate of outlet boundary, $r^{'}(k)$ is the radius of the grid on the line β, $x(ITE,k)$, $\theta(ITE,k)$ and $r(ITE,k)$ are the x,θ and r-coordinates on the trailing edge, respectively.

3.2.4 Initial Grid Generation

After the completion of grid generation on the blade surfaces and periodic boundaries, a two-dimensional grid was created on each constant radius surface considering the blade surface grid and the first grid spacings. On each constant radius surface, a Bezier curve (Faux and Pratt, 1979) was used to define a grid line between two boundaries. This Bezier curve makes the grid normal to the blade surface where the boundary condition of zero normal pressure gradient is applied.

The grid points on the Bezier curve were then distributed by using the two-end controlling function. The two-dimensional grid was smoothed by a two-dimensional elliptic smoothing routine and by stacking these smoothed grids, the initial 3-D grid was generated.

3.2.5 Elliptic Smoothing Technique

The grid generated by linear interpolation is not smooth. An elliptic smoothing routine was used to smooth the gird. This routine solves a set of coupled Poisson elliptic partial differential equations and generates smooth grid. The equations are given below:

$$\begin{aligned} \xi_{xx} + \xi_{yy} + \xi_{zz} &= \overline{P}(\xi, \eta, \zeta) \\ \eta_{xx} + \eta_{yy} + \eta_{zz} &= \overline{Q}(\xi, \eta, \zeta) \\ \zeta_{xx} + \zeta_{yy} + \zeta_{zz} &= \overline{R}(\xi, \eta, \zeta) \end{aligned} \tag{3.17}$$

These equations can be transformed into generalized coordinates by

$$\begin{aligned} \xi &= \xi(x, y, z) \\ \eta &= \eta(x, y, z) \\ \zeta &= \zeta(x, y, z) \end{aligned} \tag{3.18}$$

The Jacobian of the transformation is computed by

$$J = \det \frac{\partial(\xi, \eta, \zeta)}{\partial(x, y, z)} = \begin{vmatrix} \xi_x & \xi_y & \xi_z \\ \eta_x & \eta_y & \eta_z \\ \zeta_x & \zeta_y & \zeta_z \end{vmatrix} = \begin{vmatrix} x_\xi & x_\eta & x_\zeta \\ y_\xi & y_\eta & y_\zeta \\ z_\xi & z_\eta & z_\zeta \end{vmatrix}^{-1} \tag{3.19}$$

where $\xi_x = \frac{\partial \xi}{\partial x}$, $x_\xi = \frac{\partial x}{\partial \xi}$, etc.

The metric terms are calculated as

$$\begin{bmatrix} \xi_x \\ \xi_y \\ \xi_z \end{bmatrix} = J \begin{bmatrix} y_\eta z_\zeta - y_\zeta z_\eta \\ x_\zeta z_\eta - x_\eta z_\zeta \\ x_\eta y_\zeta - x_\zeta y_\eta \end{bmatrix} = J \begin{bmatrix} \gamma_{11} \\ \gamma_{21} \\ \gamma_{31} \end{bmatrix}$$

$$\begin{bmatrix} \eta_x \\ \eta_y \\ \eta_z \end{bmatrix} = J \begin{bmatrix} y_\zeta z_\xi - y_\xi z_\zeta \\ x_\xi z_\zeta - x_\zeta z_\xi \\ x_\zeta y_\xi - x_\xi y_\zeta \end{bmatrix} = J \begin{bmatrix} \gamma_{12} \\ \gamma_{22} \\ \gamma_{32} \end{bmatrix} \tag{3.20}$$

$$\begin{bmatrix} \zeta_x \\ \zeta_y \\ \zeta_z \end{bmatrix} = J \begin{bmatrix} y_\xi z_\eta - y_\eta z_\xi \\ x_\eta z_\xi - x_\xi z_\eta \\ x_\xi y_\eta - x_\eta y_\xi \end{bmatrix} = J \begin{bmatrix} \gamma_{13} \\ \gamma_{23} \\ \gamma_{33} \end{bmatrix}$$

Using the Jacobian of the transformation above, Equation 3.17 can be transformed into

$$\alpha_{11}\mathbf{r}_{\xi\xi} + \alpha_{22}\mathbf{r}_{\eta\eta} + \alpha_{33}\mathbf{r}_{\zeta\zeta} + 2(\alpha_{12}\mathbf{r}_{\xi\eta} + \alpha_{13}\mathbf{r}_{\xi\zeta} + \alpha_{23}\mathbf{r}_{\eta\zeta}) = \frac{-1}{J^2}(\overline{P}\mathbf{r}_\xi + \overline{Q}\mathbf{r}_\eta + \overline{R}\mathbf{r}_\zeta) \tag{3.21}$$

with

$$\mathbf{r} = \begin{bmatrix} x \\ y \\ z \end{bmatrix}$$

$$\alpha_{i,j} = \sum_{m=1}^{3} \gamma_{mi}\gamma_{mj}, \quad i = 1,2,3; j = 1,2,3$$

Where, $\overline{P}$, $\overline{Q}$ and $\overline{R}$ are the forcing functions and are used to control the grid distribution. They are defined as

$$\overline{P}(\xi,\eta,\zeta) = \overline{p}(\xi,\zeta)e^{-\alpha\eta}$$

$$\overline{Q}(\xi,\eta,\zeta) = \overline{q}(\xi,\zeta)e^{-\alpha\eta} \tag{3.22}$$

$$\overline{R}(\xi,\eta,\zeta) = \overline{r}(\xi,\zeta)e^{-\alpha\eta}$$

where α is a positive constant which determines the decay rate of the grid clustering and $\overline{p}$, $\overline{q}$ and $\overline{r}$ is determined by rewriting Equation 3.21 at the boundary, i.e; at $\eta = 0$ as follows:

$$\overline{p}\mathbf{r}_\xi + \overline{q}\mathbf{r}_\eta + \overline{r}\mathbf{r}_\zeta = \mathbf{h} \tag{3.23}$$

where

$$\mathbf{h} = \begin{bmatrix} h_1 \\ h_2 \\ h_3 \end{bmatrix} = -J^2[\alpha_{11}\mathbf{r}_{\xi\xi} + \alpha_{22}\mathbf{r}_{\eta\eta} + \alpha_{33}\mathbf{r}_{\zeta\zeta} + 2(\alpha_{12}\mathbf{r}_{\xi\eta} + \alpha_{13}\mathbf{r}_{\xi\zeta} + \alpha_{23}\mathbf{r}_{\eta\zeta})] \tag{3.24}$$

The partial derivatives of $\mathbf{r}$ with respect to ξ, η and ζ at the boundary, i.e; at $\eta = 0$, are determined by the following three relations

$$\mathbf{r}_\xi \cdot \mathbf{r}_\eta = 0$$

$$\mathbf{r}_\eta \cdot \mathbf{r}_\eta = s^2 \tag{3.25}$$

$$\mathbf{r}_\zeta \cdot \mathbf{r}_\eta = 0$$

where s is the first grid spacing at the boundary. The desired spacing and orthogonality are specified here. Expanding the equation gives

$$x_\xi x_\eta + y_\xi y_\eta + z_\xi z_\eta = 0$$

$$x_\eta x_\eta + y_\eta y_\eta + z_\eta z_\eta = s^2 \tag{3.26}$$

$$x_\zeta x_\eta + y_\zeta y_\eta + z_\zeta z_\eta = 0$$

Cramer's rule is applied to get the solution for x_η and y_η.

$$x_\eta = \frac{-z_\eta(z_\xi y_\zeta - z_\zeta y_\xi)}{x_\xi y_\zeta - x_\zeta y_\xi} = \frac{-z_\eta \gamma_{12}}{-\gamma_{32}} \tag{3.27}$$

$$y_\eta = \frac{-z_\eta(x_\xi z_\zeta - x_\zeta z_\xi)}{-(x_\zeta y_\xi - x_\xi y_\zeta)} = \frac{-z_\eta \gamma_{22}}{-\gamma_{32}} \tag{3.28}$$

Substituting x_η and y_η into the second equation in Equation 3.26 gives

$$\begin{aligned} z_\eta &= \frac{s\gamma_{32}}{\sqrt{\gamma_{12}^2 + \gamma_{22}^2 + \gamma_{32}^2}} \\ x_\eta &= \frac{s\gamma_{12}}{\sqrt{\gamma_{12}^2 + \gamma_{22}^2 + \gamma_{32}^2}} \\ y_\eta &= \frac{s\gamma_{22}}{\sqrt{\gamma_{12}^2 + \gamma_{22}^2 + \gamma_{32}^2}} \end{aligned} \tag{3.29}$$

Equation 3.29 gives the first derivative $\mathbf{r}_\eta$. The second derivatives $\mathbf{r}_{\eta\eta}$ can be derived from the Taylor series:

$$\mathbf{r}_{\eta\eta} = \frac{-7\mathbf{r}|_{j=1} + 8\mathbf{r}|_{j=2} - \mathbf{r}|_{j=3}}{2(\triangle\eta)^2} - \frac{3\mathbf{r}_\eta|_{j=1}}{\triangle\eta} \tag{3.30}$$

where j is the index in the η direction.

A multiple block, smoothing routine was used to smooth the initial grids based on the scheme described above. A smooth grid can be obtained in a few iterations by this routine.

3.3 Computational Domain for Unsteady Simulation

In the previous sections, a computational domain for steady simulation containing only a single blade was discussed. For the steady (uniform) flow condition it is assumed that the pressure variations over all the blades are the same and there are no significant flow interruptions among the blades. This type of domain is computationally efficient since it requires less memory and computing time. But for unsteady (non-uniform) inflow conditions, the flow is three dimensional and requires consideration of all of the blades to accurately investigate the unsteady nature of propeller blade loading.

An attempt was then taken to construct a domain which would contain all the blades of a propeller and the hub. The domain was created in two different ways. Firstly, by modifying *PropGGM* for each individual blade to generate separate spiral like domain and combining them together to get the full propeller. Secondly, by using the mesh transformation feature of ANSYS CFX (CFX manual, 2005). The second option was found much easier, faster and more convenient. The procedure is described in the following section.

3.3.1 Mesh Transformation

The *PropGGM* generates one blade-to-blade spiral like domain which is sufficient for uniform flow analysis. For non-uniform inflow conditions, all the blades must be considered. This was easily done by the mesh transformation editor of ANSYS CFX. The other blades and the full hub were regenerated by copying and rotating the spiral like domain. Finally, all the domains were glued together to create a continuous mesh contained in a single assembly from the multiple copies. A single domain was thus created for the entire assembly without the need of creating domain or periodic

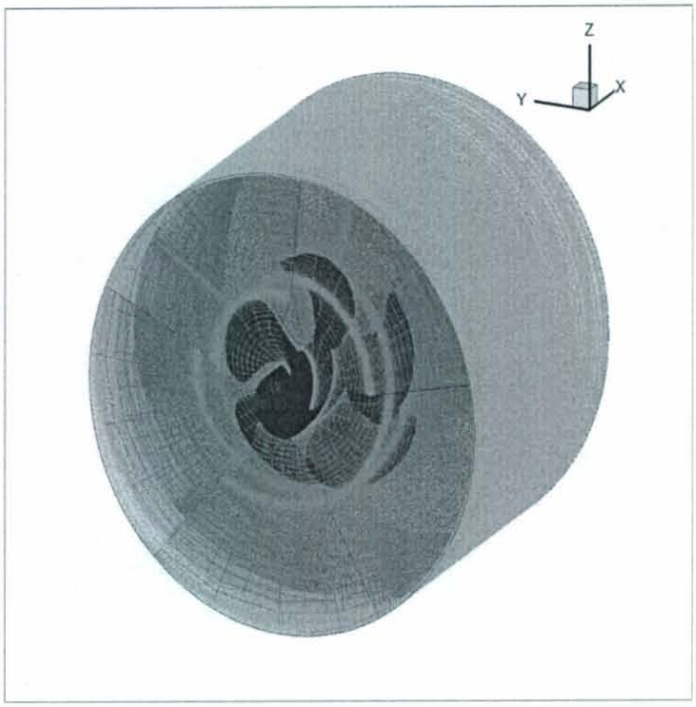

Figure 3-9: Computational domain for unsteady simulation

interfaces between each copy. Figure 3-9 shows the computational domain.

Chapter 4

Computational Method

This chapter describes the numerical method used to solve the problem. The governing equations for fluid flow are outlined first. The discretisation method of the governing equations and the solutions strategy of the descretised equations are then explained. A comprehensive summary of all turbulence models is also presented.

4.1 Governing Equations

A commercial viscous flow code, ANSYS-CFX (V11.0 and V13.0) was used for the computation. The set of equations solved by ANSYS CFX are the unsteady Navier-Stokes equations. The unsteady, three-dimensional continuity equation for compressible fluid is

$$\frac{\partial \rho}{\partial t} + \nabla \cdot (\rho \boldsymbol{U}) = 0 \tag{4.1}$$

For incompressible fluid (e.g. water) the density ρ is constant and the equation becomes:

$$\nabla \cdot (\boldsymbol{U}) = 0 \tag{4.2}$$

The Momentum conservation can be presented as:

$$\frac{\partial \rho \boldsymbol{U}}{\partial t} + \nabla \cdot (\rho \boldsymbol{U} \otimes \boldsymbol{U}) = -\nabla p + \nabla \cdot \{\rho\nu[\nabla \boldsymbol{U} + (\nabla \boldsymbol{U})^T - \frac{2}{3}\delta \nabla \cdot \boldsymbol{U}]\} + \boldsymbol{S}_M \quad (4.3)$$

where δ is the Kronecker delta function, $\boldsymbol{S}_M$ is the momentum source, $\otimes$ is the tensor product of two vectors, $\boldsymbol{U} \otimes \boldsymbol{V}$ is defined as,

$$\boldsymbol{U} \otimes \boldsymbol{V} = \begin{bmatrix} U_x V_x & U_x V_y & U_x V_z \\ U_y V_x & U_y V_y & U_y V_z \\ U_z V_x & U_z V_y & U_z V_z \end{bmatrix}$$

Additional sources of momentum are required for flows in a rotating frame of reference to account for the effects of Coriolis force and the centrifugal force. If the frame rotates at a constant angular velocity ω, the source term can be expressed as:

$$\boldsymbol{S}_{M,rot} = -2\rho\omega \times \boldsymbol{U} - \rho\omega \times (\omega \times \boldsymbol{r}) \quad (4.4)$$

where the first term represents the Coriolis force and the second term is the centrifugal force, $\boldsymbol{r}$ is the location vector and $\boldsymbol{U}$ is the relative frame velocity, i.e., the rotating frame velocity for a rotating frame of reference. The final form of the momentum equation becomes:

$$\frac{\partial \rho \boldsymbol{U}}{\partial t} + \nabla \cdot (\rho \boldsymbol{U} \otimes \boldsymbol{U}) = -\nabla p + \nabla \cdot \{\rho\nu[\nabla \boldsymbol{U} + (\nabla \boldsymbol{U})^T - \frac{2}{3}\delta \nabla \cdot \boldsymbol{U}]\} - 2\rho\omega \times \boldsymbol{U} - \rho\omega \times (\omega \times \boldsymbol{r}) \quad (4.5)$$

The total energy equation can be expressed as:

$$\frac{\partial (\rho h_{tot})}{\partial t} - \frac{\partial p}{\partial t} + \nabla \cdot (\rho \boldsymbol{U} h_{tot}) = \nabla \cdot (\lambda \nabla T) + \nabla \cdot (\boldsymbol{U} \cdot \tau) + \boldsymbol{U} \cdot \boldsymbol{S}_M + \boldsymbol{S}_E \quad (4.6)$$

where h_{tot} is the total enthalpy. The term $\nabla \cdot (\boldsymbol{U} \cdot \tau)$ represents the viscous work due to the viscous stresses and the term $\boldsymbol{U} \cdot \boldsymbol{S}_M$ represents the work due to external momentum sources, and $\boldsymbol{S}_E$ is the energy source.

The remaining unknown thermodynamics variables (ρ, P, i and T) are linked together through the assumption of hydrodynamic equilibrium and are expressed by only two state variables. This expression is known as the equation of state. For an incompressible fluid, where the density is constant, there is no need for the state equation. The flow field can often be solved by considering only the mass conservation and momentum equations. The energy equation only needs to be solved alongside the others if the problem involves any heat transfer (Versteeg and Malalasekera, 1995).

For turbulent flows like propeller tip vortex flows, the Navier-Stokes (N-S) equations have to be modified to produce the Reynolds Averaged Navier-Stokes (RANS) equations by employing averaged and fluctuating quantities. The resulting equations then become:

$$\frac{\partial \rho}{\partial t} + \nabla \cdot (\rho \boldsymbol{U}) = 0 \tag{4.7}$$

$$\frac{\partial \rho \boldsymbol{U}}{\partial t} + \nabla \cdot (\rho \boldsymbol{U} \otimes \boldsymbol{U}) = \nabla \cdot \tau - \rho \overline{\boldsymbol{u} \otimes \boldsymbol{u}} + S_M \tag{4.8}$$

where τ is the molecular stress tensor and $\rho \overline{\boldsymbol{u} \otimes \boldsymbol{u}}$ are the Reynolds stresses. These stresses are modelled by introducing turbulence model to enclose the governing equations. Details of the turbulence models are described in Section 4.4.

4.2 Discretisation of Governing Equations

So far we have seen that the flow phenomena are governed by partial differential equations. Analytical solutions to these equations are only available for the simplest of flows, under ideal conditions. To solve real flow problems, a numerical approach must be adopted whereby the equations are replaced by algebraic approximations and the process is known as numerical discretisation. This section describes this descretisation method used for the simulation (Versteeg and Malalasekera, 1995).

There are significant commonalities between the various governing equations and can be written in the following general form:

$$\underbrace{\frac{\partial(\rho\phi)}{\partial t}}_{\text{Rate of change term}} + \underbrace{div(\rho\phi\mathbf{u})}_{\text{Convective term}} = \underbrace{div(\Gamma grad\phi)}_{\text{Diffusive term}} + \underbrace{S_\phi}_{\text{Source term}} \tag{4.9}$$

where ϕ is the variable of interest, Γ is the diffusion coefficient. The Equation 4.9 is known as transport equation since it describes various transport processes of dependent variables. This equation represents different aspects of the fluid motion. The convection term represents the flux of ϕ convected by the mass flow rate $\rho\mathbf{u}$, the diffusion term represents the random motion of particles and the source term represents the generation and destruction of ϕ. The non-linear nature of the convective term makes it difficult to solve the equations directly, that is, as a set of simultaneous equations. An iterative solution method is the only way to solve these equations. The governing equations are discretised, that is, approximately linearised to obtain the algebraic equations and are solved at discrete points throughout the domain.

A variety of techniques, including and not limited to finite difference and finite volume methods, are available to perform this numerical discretisation but a finite volume approach is adopted here. A brief description of the method is given below.

4.2.1 Finite Volume Method

The finite volume method is probably the most popular descretization method used in CFD. This method draws on ideas from both finite element and the finite difference discretisation techniques. In this approach the computational domain is discretized into finite control volumes, also known as cells. The governing equations are integrated over each control volume which utilises the conservation principles directly. The integral form of Equation 4.9 over a control volume gives

$$\frac{\partial}{\partial t}\int_{CV}\rho\phi dV + \int_{A}\mathbf{n}\cdot(\rho\phi\mathbf{u})dA = \int_{A}\mathbf{n}\cdot(\Gamma grad\phi)dA + \int_{CV}S_{\phi}dV \qquad (4.10)$$

The Equation 4.10 represents the flux balance in a control volume where the left hand side represents the rate of change of ϕ and net convective flux and right hand side gives the the net diffusive flux and the generation or destruction of the property ϕ. These fluxes are evaluated by various numerical schemes which are discussed in the following sections.

The main advantage of the finite volume method is that the spatial discretisation is carried out directly in the physical space. Thus, there are no problems with any transformation between coordinate systems, like in the case of the finite difference method. Compared to the finite difference method, another advantage of the finite volume method is that it is flexible to implement on both structured and unstructured grids. This makes finite volume method suitable for the treatment of flows in complex geometries.

4.2.2 Discretisation of the Domain

Older CFD codes used a staggered mesh approach where the scalar variables were calculated at the cell centres and the vector variables, i.e. the velocities, at the cell faces. But recent codes, such as CFX, use a co-located (non-staggered) grid layout

where the values of all variables are calculated at the centre of each control volume. This approach is better than the previous one since it requires only one mesh to get the values of all the variables. In a complicated geometry, where curvilinear (non-rectangular) meshes are used, application of co-located grid is easier because of its simplicity. However, this method leads to a decoupling of the velocity and pressure fields giving a 'checkerboard' effect. This is overcome by Rhie-Chow (Rhie and Chow, 1982) interpolation algorithm, which is further modified by Majumdar (CFX manual, 2005) to remove the dependence of the steady-state solution on the timestep size.

4.2.3 Advection Terms

Advection terms can be approximated with different advection schemes available in CFX. All the schemes have some advantages and disadvantages. For example, the first order accurate upwind differencing scheme gives the most robust performance of the solver but it suffers from numerical diffusion. On the other hand, the second order accurate scheme is free from the diffusion problem but sometimes it gives non-physical results. A blend of these two schemes can be achieved by the use of the high resolution scheme, which was implemented in this simulation. A blend factor (β) is sent in a range of 0.0 for fully first order to 1.0 for fully second order schemes. The blend factor values vary throughout the domain based on the local solution field. If the variable gradients is low in a flow region, the blend factor will be close to 1.0, but will be closer to 0.0 where the gradients change sharply. In other words, the scheme is fully second order as long as there are no discontinuities in the flow. It drops to first order to keep the solution bounded. A central difference advection scheme is also available to CFX but it is reserved for large eddy simulation turbulence model only. The third order accurate QUICK scheme is also available in CFX but not listed in the main options and perhaps this is not recommended for general use.

4.2.4 Diffusion Terms

The reasonable way to discretise diffusion terms is to employ a central difference scheme because of the physical nature of the viscous flux. Thus, their discretisation on structured grids is straightforward. On unstructured triangular or tetrahedral grids, the viscous fluxes are best approximated by following the standard finite element approach. CFX also uses this approach by employing shape functions to evaluate the derivatives for all the diffusion terms.

4.2.5 Transient terms

The transient term of Equation (4.10) can be split into terms as follows:

$$\frac{\partial}{\partial t}\int_{CV}\rho\phi dV = V(\rho^0\frac{\partial\phi}{\partial t} + \phi\frac{\partial\rho}{\partial t}) \tag{4.11}$$

The time derivatives of Equation (4.11) can be approximated by either the first order Backward Euler scheme or by a second order Backward Euler scheme. The first order scheme is robust, fully implicit, bounded, conservative in time, and does not create a timestep limitation. But since it is only first order accurate, it suffers from numerical diffusion in time, similar to the numerical diffusion experienced with the Upwind Difference Scheme for discretising the advection term. On the other hand, the second order scheme is also robust, implicit, conservative in time, and does not create a time step limitation, but it is not bounded and may hence create some nonphysical overshoots or undershoots in the solution. However, all the simulations were done with this Second Order Backward Euler scheme.

4.3 Solution Strategy of the Discretised Equations

There is no equation (transport or other) for pressure and this aspect is therefore treated differently. A constraint is set on the solution of the flow field in that when

the correct pressure is substituted in the momentum equations, the resulting velocity field satisfies mass continuity. ANSYS CFX uses segregated solvers which solve the momentum equations using a guessed pressure and obtain a pressure correction relation. This 'guess-and-correct' approach of the linear solver requires a large number of iterations. A coupled solver solves the hydrodynamic equations (for u, v, w, p) as a single system with a fully implicit discretisation method. This reduces the number of iterations to achieve the convergence criteria. The discrete system of linearised equations are solved by an Incomplete Lower Upper (ILU) factorisation technique accelerated by algebraic Multigrid (MG) method (Raw, 1996).

4.4 Turbulence Modeling

Turbulence modelling is another important issue to consider especially when the simulation deals with the fluctuating flows like propeller flows. A screw propeller induces highly rotating flow and entails a tip vortex, which causes turbulence in the tip vortex region. A viable tool then required to represent this turbulence effect.

The random nature of a turbulent flow can be explained by introducing averaged and fluctuating components. For example, a velocity $u(t)$ can be divided into an average component U and a fluctuating component $u^{'}(t)$

$$u(t) = U + u^{'}(t) \tag{4.12}$$

Thus, it requires modification of the original unsteady Navier-Stokes equations, considering the averaged and fluctuating quantities to produce the Reynolds Averaged Navier-Stokes (RANS) equations. These equations are obtained by using the statistical averaging procedure. This averaging procedure introduces additional stresses in the fluid known as 'Reynolds stresses' and need to be modelled in order to achieve 'closure'. Turbulence models provide the model for the computation of the

Reynolds stresses. There are several turbulence models available to CFX which can be categorized into two classes, eddy viscosity models and Reynolds stress models. They are discussed below.

4.4.1 Eddy Viscosity Turbulence Models

These turbulence models are based on the hypothesis that the Reynolds stresses are proportional to mean velocity gradients and Eddy (turbulent) viscosity can be related by the gradient diffusion hypothesis.

$$-\rho\overline{\mathbf{u}\otimes\mathbf{u}} = \rho\mu_t[\nabla\mathbf{U} + (\nabla\mathbf{U})^T] - \frac{2}{3}\delta\rho(k + \mu_t\nabla\cdot\mathbf{U}) \tag{4.13}$$

where, δ is the Kronecker's delta and μ_t is the eddy viscosity or turbulent viscosity, which has to be modeled. At the same time the eddy diffusivity, Γ_t also has to be modeled which is computed based on the assumption that the Reynolds fluxes of a scalar are linearly related to the mean scalar gradient.

$$-\rho\overline{u\phi} = \Gamma_t\nabla\phi \tag{4.14}$$

The eddy viscosity models are distinguished by the manner they prescribe eddy viscosity and eddy diffusivity. The various eddy viscosity models are described below.

Zero Equation Model

In this model the eddy viscosity is computed from the mean velocity and a geometric length scale using an empirical formula as follows:

$$\mu_t = \rho f_\mu U_t l_t \tag{4.15}$$

where, f_μ is a proportionality constant and l_t is the length scale proposed by Prandtl and Kolmogorov. Since no transport equation is involved, this model named as 'zero'

equation model. The advantage of this model is its simplicity to implement and cheap in terms of computing time. But since it is based on empirical formulas, the model is not reliable.

Two Equation Turbulence Models

These models solve two separate transport equations, one for turbulent velocity scale and another for turbulent length scale. The product of velocity and length scale are then used to model turbulent viscosity, μ_t. The turbulent velocity scale is computed from the turbulent kinetic energy, k, which is provided from the solution of its transport equation. And the the turbulent length scale is estimated from the turbulent kinetic energy, k, and its dissipation rate, ϵ.

1. $k-\epsilon$ model

This model predicts the turbulence viscosity from following relation:

$$\mu_t = c_\mu \rho \frac{k^2}{\epsilon} \tag{4.16}$$

where C_μ is a constant. The values of k and ϵ are solved from the following differential transport equations:

$$\frac{\partial(\rho k)}{\partial t} + \nabla \cdot (\rho \mathbf{U} k) = \nabla \cdot [(\mu + \frac{\mu_t}{\sigma_k})\nabla k] + P_k - \rho\epsilon \tag{4.17}$$

$$\frac{\partial(\rho \epsilon)}{\partial t} + \nabla \cdot (\rho \mathbf{U} \epsilon) = \nabla \cdot [(\mu + \frac{\mu_t}{\sigma_\epsilon})\nabla \epsilon] + \frac{\epsilon}{k}(c_{\epsilon 1} P_k - c_{\epsilon 2}\rho\epsilon) \tag{4.18}$$

where the constant coefficients $c_\mu = 0.09$, $c_{\epsilon 1} = 1.44$, $c_{\epsilon 2} = 1.92$, $\sigma_k = 1.0$ and $\sigma_\epsilon = 1.3$. P_k is the turbulence production due to viscous and buoyancy forces, which is modeled as:

$$P_k = \mu_t \nabla \mathbf{U} \cdot (\nabla \mathbf{U} + \nabla \mathbf{U}^T) - \frac{2}{3}\nabla \cdot \mathbf{U}(3\mu_t \nabla \cdot \mathbf{U} + \rho k) + P_{kb} \tag{4.19}$$

Due to the excellent performance in many practical flows, this model is well established and widely validated. However, poor performances are reported in a variety of important cases like confined flows, flow with large extra strains, and in rotating flows.

2. RNG $k-\epsilon$ model

This model shares the same transport equations as those for standard $k-\epsilon$ equation. The only difference is the model constants. The constant $C_{\epsilon 1}$ is replaced by the strain dependent correction term function $C_{\epsilon 1RNG}$ where,

$$C_{\epsilon 1RNG} = 1.42 - f_\eta \tag{4.20}$$

where,

$$f_\eta = \frac{\eta(1-\frac{\eta}{4.38})}{(1+\beta_{RNG}\eta^3)}$$

The details of the other constants can be found in CFX manual (2005).

3. $k-\omega$ model

This model, developed by Wilcox (1986), assumes that the turbulence viscosity is linked to the turbulence kinetic energy, k, and turbulent frequency, ω, via the relation:

$$\mu_t = \rho\frac{k}{\omega} \tag{4.21}$$

The transport equations for k and ω are:

$$\frac{\partial(\rho k)}{\partial t} + \nabla\cdot(\rho\mathbf{U}k) = \nabla\cdot[(\mu+\frac{\mu_t}{\sigma_k})\nabla k] + P_k - \beta'\rho k\omega \tag{4.22}$$

$$\frac{\partial(\rho\omega)}{\partial t} + \nabla\cdot(\rho\mathbf{U}\omega) = \nabla\cdot[(\mu+\frac{\mu_t}{\sigma_\omega})\nabla\omega] + \alpha\frac{\omega}{k}P_k - \beta\rho\omega^2 \tag{4.23}$$

with $\alpha = 5/9$, $\beta = 0.075$, $\beta' = 0.09$, $\sigma_k = 2$ and $\sigma_\omega = 2$, and P_k is calculated as in the

$k-\epsilon$ model. This model is more robust and more accurate then $k-\epsilon$ model since it does not require any non-linear damping functions. The near wall performance of this model is also very attractive.

4. The Baseline (BSL) $k-\omega$ Model

This is a blended form of Wilcox $k-\omega$ model and modified $k-\epsilon$ model to eliminate the extreme sensitivity to freestream conditions of the Wilcox model. The $k-\epsilon$ model is transformed to a $k-\omega$ formulation and multiplied by a blending function $1-F_1$. The Wilcox model is multiplied by the function F_1 where F_1 is equal to one near the surface and switches over to zero inside the boundary layer. The corresponding k and ω equations are then added to get the BSL model.

5. The Shear Stress Transport (SST) Model

This model can be called as a improved version of BSL model. The BSL model combines the advantages of the $k-\omega$ and the $k-\epsilon$ model, but it fails to predict flow separation accurately. The reasons were revealed by Menter (1994) and the main reason is that both models do not account for the transport of the turbulent shear stress which results in an over prediction of the eddy-viscosity. Menter then introduces limiters where the eddy viscosity is limited to give improved performance in flows with adverse pressure gradients and wake regions. The turbulent kinetic energy production is limited to prevent the build-up of turbulence in stagnation regions. The limiter can be expressed as:

$$\mu_t = \frac{\rho a_1 k}{max(a_1\omega, SF_2)} \tag{4.24}$$

where F_2 is a blending function similar to F_1 in BSL model, a_1 is a constant and $S = \sqrt{2S_{ij}S_{ij}}$.

K-epsilon One Equation Model

This simple one equation model, developed by Menter (1994), is derived directly from the $k-\epsilon$ model and is therefore named the $(k-\epsilon)_{1E}$ model. The model contains a destruction term, which accounts for the structure of turbulence. The eddy viscosity is computed from:

$$\mu_t = \rho\nu_t^{'} \tag{4.25}$$

where, $\nu_t^{'}$ is the turbulent kinematic eddy viscosity. This model includes damping functions to catch the low Reynolds effect.

4.4.2 Reynolds Stress Turbulence (RSM) Models

These models do not use the eddy viscosity hypothesis, but solve all transport equations for all components of the Reynolds stress tensor and the dissipation rate. The transport equation for the Reynolds stresses is:

$$\frac{\partial\rho\overline{\mathbf{u}\otimes\mathbf{u}}}{\partial t} + \nabla\cdot(\rho\mathbf{U}\otimes\overline{\mathbf{u}\otimes\mathbf{u}}) = (P+\phi+\nabla\cdot((\mu+\frac{2}{3}c_s\rho\frac{k^2}{\epsilon})\nabla\overline{\mathbf{u}\otimes\mathbf{u}}) - \frac{2}{3}\delta\rho\epsilon) \tag{4.26}$$

where ϕ is the pressure-strain correlation and P is the production term, given by:

$$P = -\rho(\overline{\mathbf{u}\otimes\mathbf{u}}(\nabla\mathbf{U})^T + (\nabla\mathbf{U})\overline{\mathbf{u}\otimes\mathbf{u}}) \tag{4.27}$$

The pressure strain interaction is most important, but most difficult to model accurately. This interaction reduces anisotropy of turbulent eddies and therefore it requires additional corrections.

The exact production term and the stress anisotropies theoretically make Reynolds Stress models more suited to complex flows. But it requires large computing

time and in practice it poorly predicts some flows (for example, axis asymmetric jets, unconfined re-circulating flows) due to the identical problems with the ϵ equation.

There are three types of standard Reynolds stress models available. These are known as LRR-IP, LRR-QI and SSG. Each model has different model constants. In the LRR-IP and LRR-QI models, developed by Launder et al. (1975), the pressure-strain correlation is linear. IP stands for Isotropization of Production, and QI stands for Quasi-Isotropic. On the other hand, SSG model, developed by Speziale (1991), uses a quadratic relation for the pressure-strain correlation.

There are other two types of Reynolds stress models available, the Omega Reynolds Stress and Baseline (BSL) Reynolds Stress models. These models are based on ω equation and are used for a more accurate near wall treatment. The two models relate to each other in the same way as the two equation $k - \omega$ and BSL models do.

Chapter 5

Validation Studies

This chapter has two parts: the first part describes the research findings of the steady state tip vortex flow while the second part deals with the results obtained from the unsteady simulation. Validation studies were carried out for both steady and unsteady cases.

5.1 Steady Case

The steady state tip vortex was previously computed and validated by Liu (2009). An extension of her work was conducted to investigate the effect of turbulence modeling on the computation of tip vortex flow with eddy viscosity turbulence models and Reynolds stress models. The pressure coefficient on the blade surface and the propeller thrust and torque coefficient were also computed. The predictions agree well with the measured velocity components but underpredict the thrust and torque coefficients. Additional experiments were then conducted to reveal the reason and a modification of the previous numerical experiment (Liu, 2009) was performed.

To clearly explain the findings of this experiment, the previous numerical experiment (Liu, 2009) is also summarized as follows.

5.1.1 Simulation Technique

The validation studies were carried out for the DTMB 5168 propeller model at the advance coefficient $J = 1.1$. The propeller model geometry and operational conditions are shown in Table 5.1. In the computation, the water density and viscosity were set to $\rho_{water} = 997kg/m^3$ and $\mu_{water} = 8.89 \times 10^{-4}kgm^{-1}s^{-1}$, respectively.

Table 5.1: Principal Characteristics of DTMB 5168

Designation	Values
Diameter $(inch)$	15.856
Inflow velocity $(inch/s)$	421.44
Chord length at $0.7R$ $(inch)$	6.897
Advance coefficient	1.1
Rotation speed (RPS)	24.163
Combined velocity at $0.7R$ $(inch/s)$	942.12
Reynolds number	4.2×10^6

Computational Domain

The spiral like computational domain, as shown in Figure 5-2, was created by setting the inlet boundary at one propeller radius upstream and the outlet boundary one diameter downstream. The outer boundary in the radial direction was located at one propeller diameter (Liu, 2009).

Primary/secondary coordinate system

A primary/secondary coordinate system, as shown in Figure 5-1, was used to better describe the tip vortex structure. In this system, the primary velocity, V_s, is defined in the axial-tangential $x-t$ plane at the propeller pitch angle, ϕ. Tangential velocity, V_c, and radial velocity, V_r, are on the secondary flow plane normal to the primary velocity. The primary and tangential velocities are defined as:

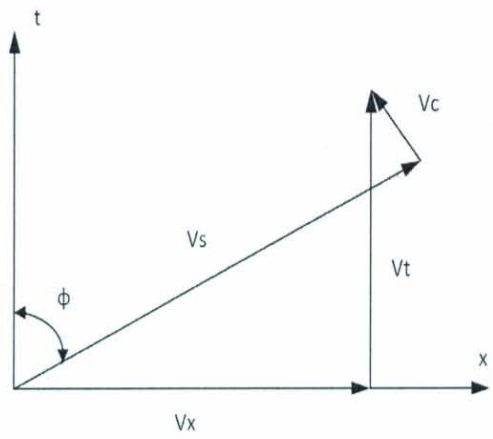

Figure 5-1: Primary and secondary coordinate system

$$V_s = V_x \sin\phi + V_t \cos\phi$$

$$V_c = -V_x \cos\phi + V_t \sin\phi \tag{5.1}$$

The center of the vortex core is defined at the location with minimum V_s and is denoted by $\theta = 0$ in the figures.

Boundary Condition

The boundary conditions were specified as follows. A no-slip wall condition was applied on the blades and the hub surfaces (denoted by black in Figure 5-2) . A free stream condition was applied on the inlet boundary and the outer surface in the span-wise direction (denoted by green). The flow rate was specified at the outlet boundary. Rotational periodic conditions were applied on the periodic boundaries by the Fluid-Fluid Interface Modeling in ANSYS CFX.

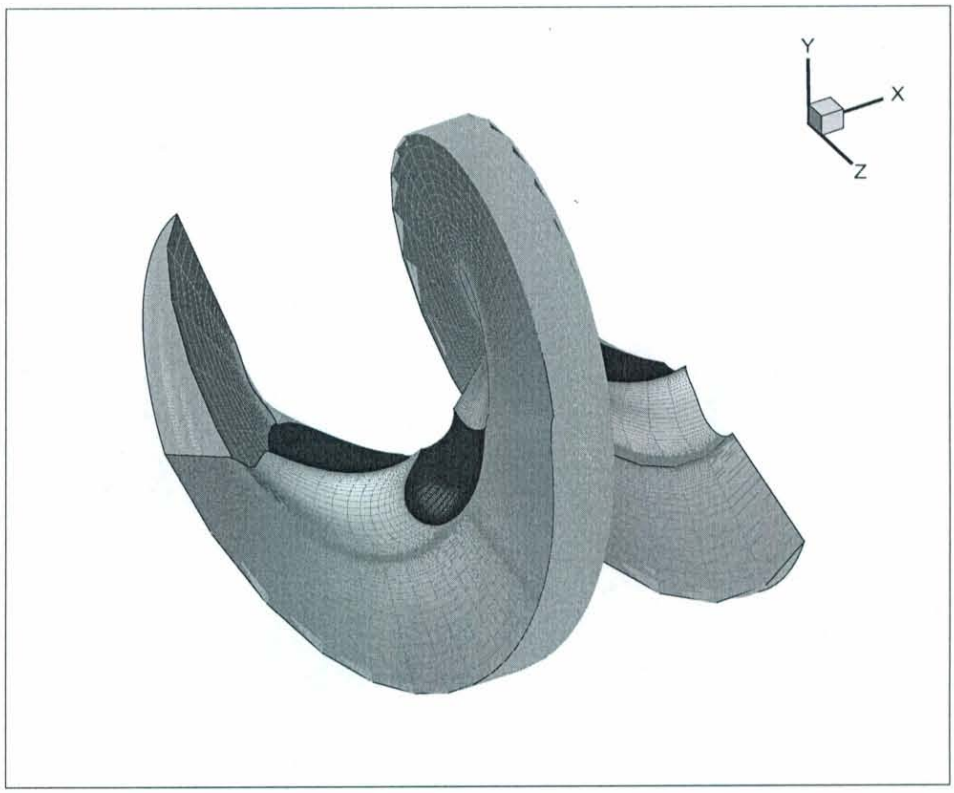

Figure 5-2: Computational domain of DTMB 5168

Simulation Condition

Advection terms were discretised by the high resolution scheme. Viscous terms were treated by employing the central difference scheme. The timestep size was determined automatically by CFX. The convergence criterion was set to the RMS residual to 1×10^{-04}. To achieve the desired convergence, a total of $10,000$ iterations were required.

5.1.2 Convergence Tests

Before conducting the simulation, convergence tests were performed to find out the grid sensitivity of the domain on the solution and to select the least number of iterations. The grid sensitivity was done by Liu (2009). To maintain the sequence, the detail of the test is explained here.

Three computational grids, Grid I, Grid II and Grid III, were used for the convergence test. A summary of the three sets of grids is given in Table 5.2.

Table 5.2: Summary of Grids

	Grid I	Grid II	Grid III
Number of grids	171×101×111	211×101×111	231×111×121
y^+ on blade	7.5	2.08	1.0
y^+ on hub	7.5	2.43	1.0

The computed axial, tangential and radial velocities (V_x, V_t and V_r, respectively) in the tangential direction across the tip vortex centre at the location $x = 0.2386R$ were compared with the experimental data (Chesnakas and Jessup, 1998). Here, R is the propeller radius. From the test, it was found that grid I with largest first grid spacing led to a better prediction. The first grid spacing on the blade and hub was 3.6×10^{-4} inches which represents an equivalent non-dimensional wall distance (y^+) of 7.5. Note that a small first grid spacing may lead to grid cells with huge Jacobian values, which will cause the ANSYS CFX solver not to converge. Details of the test

can be found in Liu (2009).

Another convergence test was carried out to find the effect of grid resolution on the computing time of simulation. Using the SST turbulence model, the three sets of grids were compared in Figure 5-3. It was found that Grid II reached to the converged solution quickly compared to the other two. But within 500 iterations, all types of grid converged and merged at the same point. Apparently, no significant effect was found.

Based on the above mentioned convergence studies, Grid I was chosen for further studies. The computational domain contains an $H-H$ type grid with more than 1.9 million grid points. This domain was used to investigate the effect of turbulence models on the predictions of V_x, V_t and V_r across the tip vortex center in the tangential direction at $x = 0.2386R$ (R is the propeller radius).

5.1.3 Effect of Turbulence Modeling

An investigation was done to show the effect of turbulence modeling on the vortex flow computation. Various eddy viscosity and Reynolds stress turbulence models were employed in the investigation. The eddy viscosity models include zero-, one- and two-equation turbulence models. The simple one-equation model, $(k-\epsilon)_{1E}$, derived from the $(k-\epsilon)$ model, was used. In the two-equation eddy viscosity turbulence models, $(k-\epsilon)$, (RNG $k-\epsilon$), and the blended $(k-\omega)SST$ models were chosen. Three types of standard Reynolds stress models based on the $\epsilon-$ equation and two other $\omega-$ based Reynolds stress models were employed. The three standard models were SSG Reynolds Stress Model (RSM) and the Launder-Reece-Rodi models (LRR): LRR-IP and LRR-QI. The other two $\omega-$ based models were Baseline (BSL) RSM and the Omega Reynolds stress model. Among the above mentioned models, $(k-\epsilon)$, SST, SSG RSM and BSL RSM models were previously employed by Liu (2009).

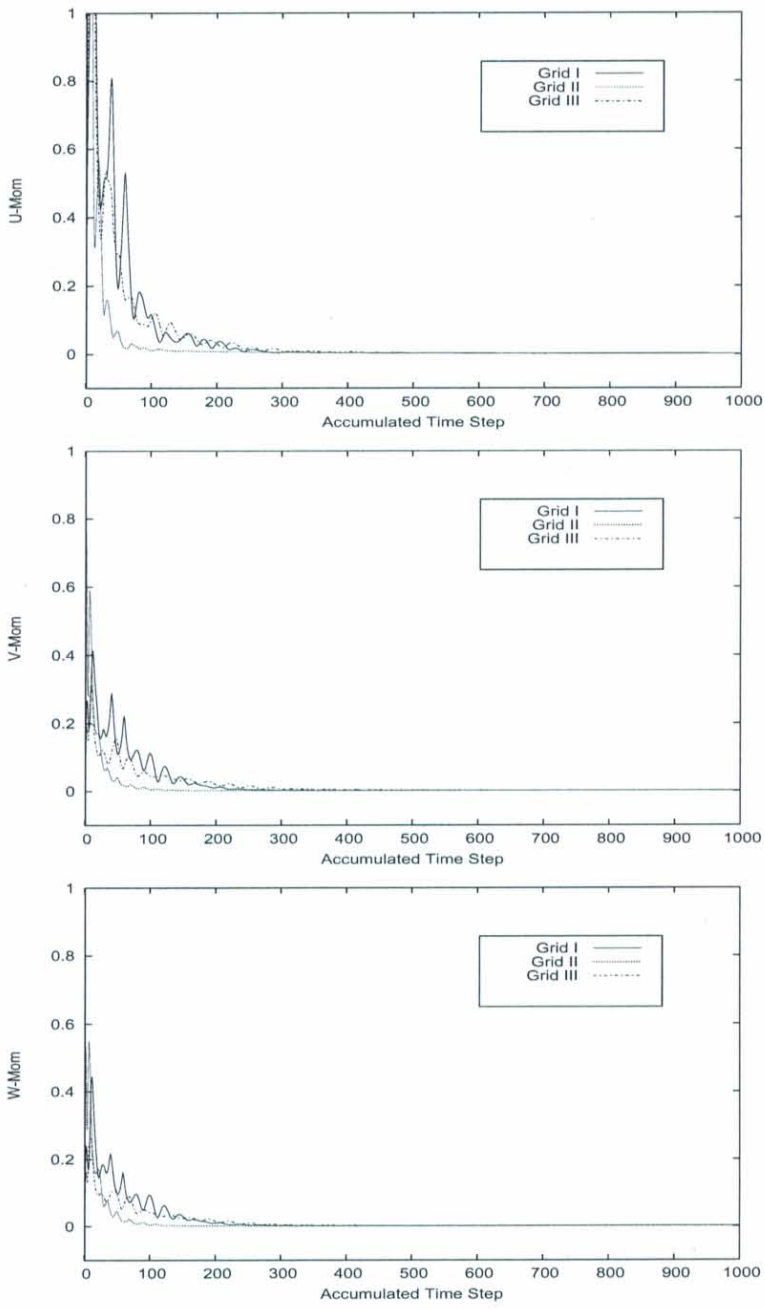

Figure 5-3: Effect of grid resolution on computing time

Velocities across the tip region

The velocities V_x, V_t and V_r across the tip vortex centre were compared with the the experimental data and with the numerical data by Hsiao and Pauley (1999) to show the effect of turbulence models on the velocity predictions. The post processor of the program *PropGGM* was modified to make it compatible with the ANSYS CFX. A further modification was done to non-dimensionalize the velocities. Figure 5-4 presents the solutions based on the eddy viscosity turbulence models and Figure 5-5 gives the computed results based on the Reynolds stress models. In the figures, the first valley corresponds to the wake and the second valley is associated with the tip vortex. In the work of Hsiao and Pauley (1999), the computations were carried out using INS3D-UP with a one-equation Baldwin-Barth turbulence model. The computational domain had 2.36 million structured grids.

For axial velocity, V_x, in Figure 5-4, $k-\epsilon$ and the SST turbulence models predict better at the vortex location while the wake valley is better predicted by the zero-equation, the $(k-\epsilon)_{1E}$ and the RNG $k-\epsilon$ models. For V_t, the computed results with the $k-\epsilon$ and the SST turbulence models agree better with the experimental data than those by other eddy viscosity models at both the wake valley and at the vortex location. The computed results for radial velocity component, V_r, gives poor predictions compared to the other components, V_x and V_t. The computed results with various turbulence models are similar at the vortex location and at the wake region. However, zero-equation model, the $(k-\epsilon)_{1E}$ model and the RNG $k-\epsilon$ model match well at the wake valley with the numerical results of Hsiao and Pauley (1999). In fact, in Figure 5-4, it can also be observed that the predictions by the zero-equation model, the $(k-\epsilon)_{1E}$ model and the RNG $k-\epsilon$ model are similar and they are slightly different at the vortex location.

Similar observations also found for the predicted velocities using various Reynolds

stress models in Figure 5-5. The SSG and BSL Reynolds stress models in general give better predictions of V_x and V_t at the vortex location. LRR-IP, LRR-QI and omega Reynolds stress models give similar predictions. So far, it is observed that the $k-\epsilon$ and the SST turbulence models from eddy viscosity models and the SSG and the BSL turbulence models from Reynolds stress models cope well with the experimental results.

A further comparison is shown in Figure 5-6 for the computed velocities with the $k-\epsilon$ and the SST turbulence models and the SSG and the BSL turbulence models to compare the predictions by eddy viscosity and Reynolds stress models. It can be seen from the figure that the predictions by two-equation eddy viscosity models and the Reynolds stress models are similar. In the plot of V_x, ANSYS CFX with the $k-\epsilon$, the SST, the BSL and the SSG turbulence models give better predictions of the valley shape at the vortex location than INS3D-UP while the wake valley is better predicted by INS3D-UP. For V_t, the computed results by ANSYS CFX with two-equation models and Reynolds stress models agree better with the experimental data than those by INS3D-UP. For V_r, the computed results by ANSYS CFX with various turbulence models are similar and none of them are better than the the results by INS3D-UP with one equation model at the vortex valley.

The contour plot of three computed velocity components, V_x, V_t and V_r at $x/R = 0.2386$ for the $k-\epsilon$ model and the BSL Reynolds stress model were compared with the experimental data by Chesnakas and Jessup (1998) in Figures 5-7 to 5-9. It can be shown that the predicted velocity field by ANSYS CFX is visually similar to the experimental one. The differences between results by the two turbulence models are insignificant. The additional contour plots for other turbulence models are given in the Appendix.

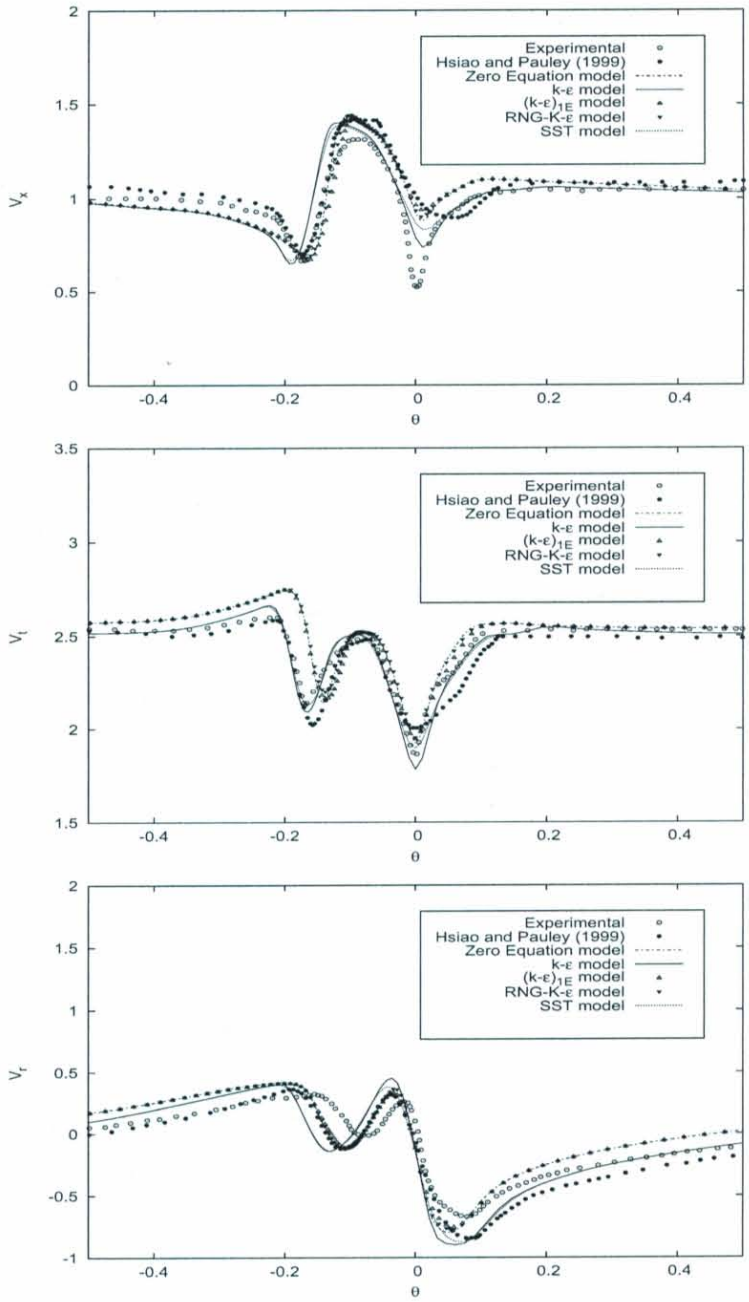

Figure 5-4: Vx, Vt, Vr across the tip vortex center at $x/R = 0.2386$ computed with eddy viscosity turbulence models

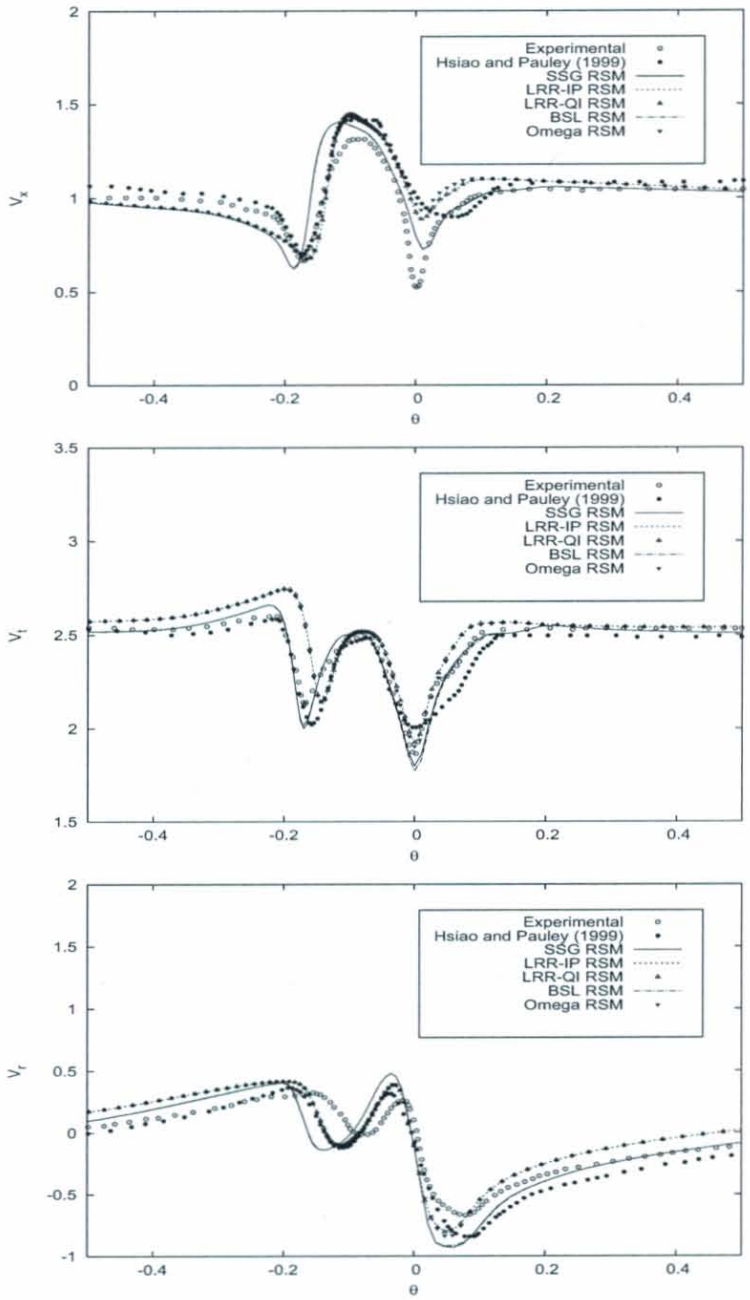

Figure 5-5: Vx, Vt, Vr across the tip vortex center at $x/R = 0.2386$ computed with Reynolds stress models

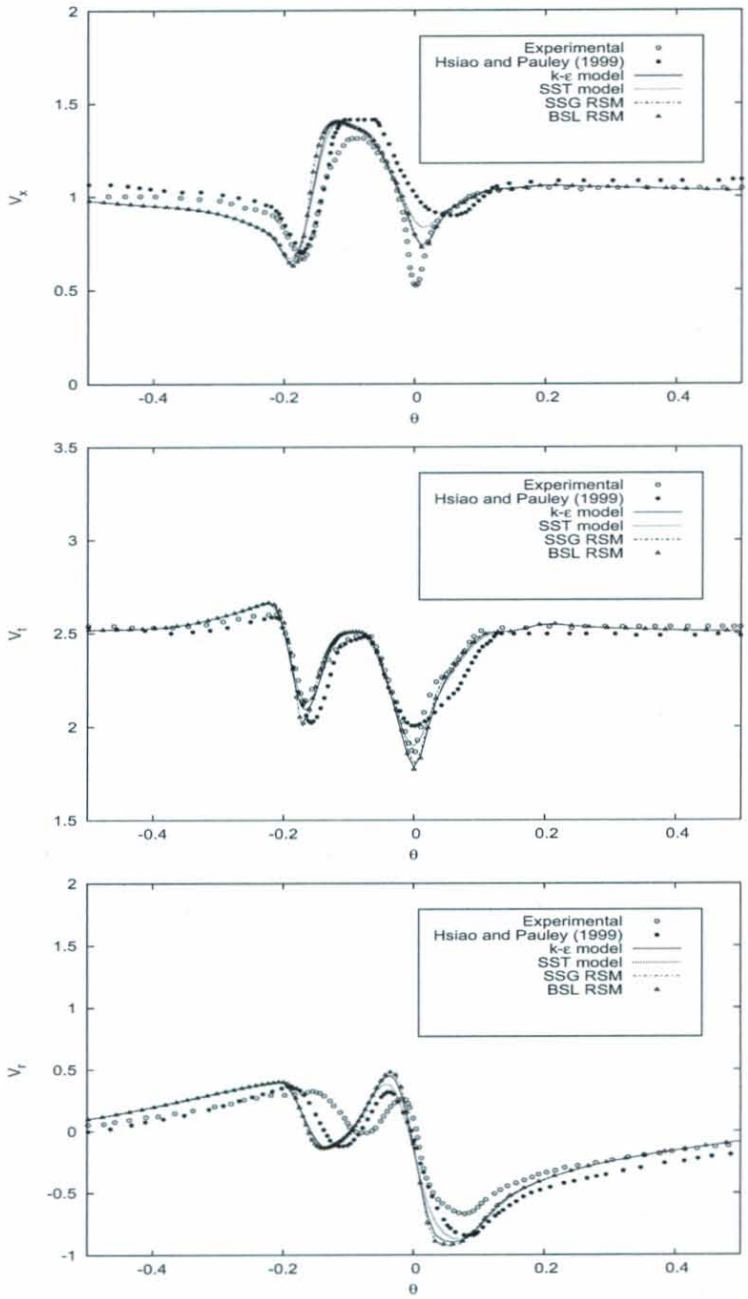

Figure 5-6: Comparison of Vx, Vt, Vr across the tip vortex center at $x/R = 0.2386$ with Reynolds stress models and eddy viscosity models

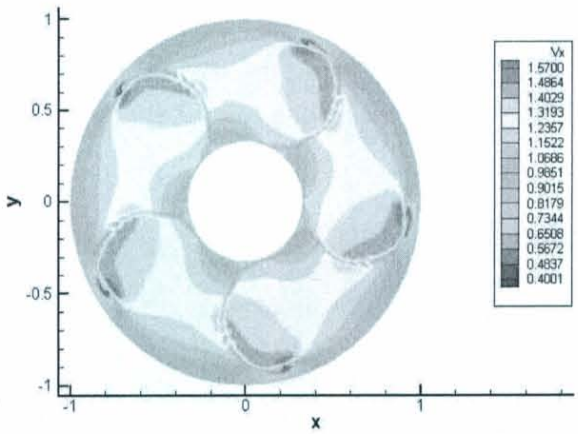

(a) Experimental results by Chesnakas and Jessup (1998)

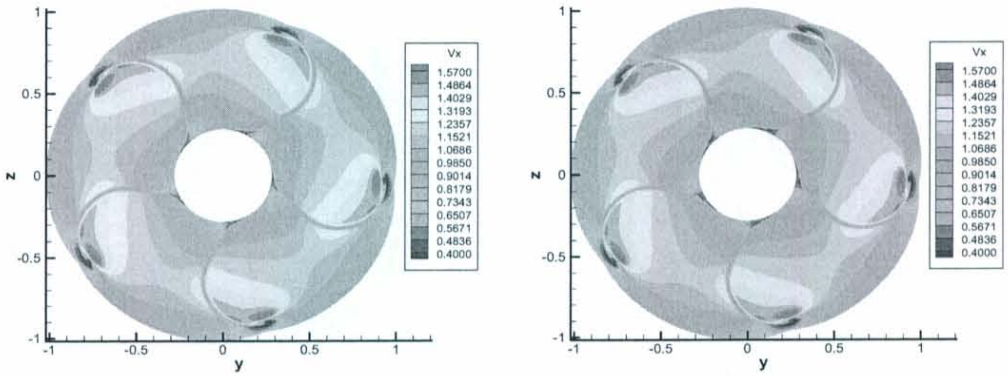

(b) $k - \epsilon$ model

(c) BSL RSM model

Figure 5-7: Axial velocity V_x at $x/R = 0.2386$

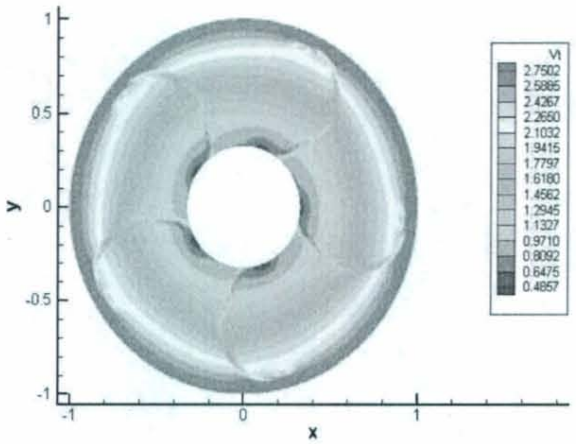

(a) Experimental results by Chesnakas and Jessup (1998)

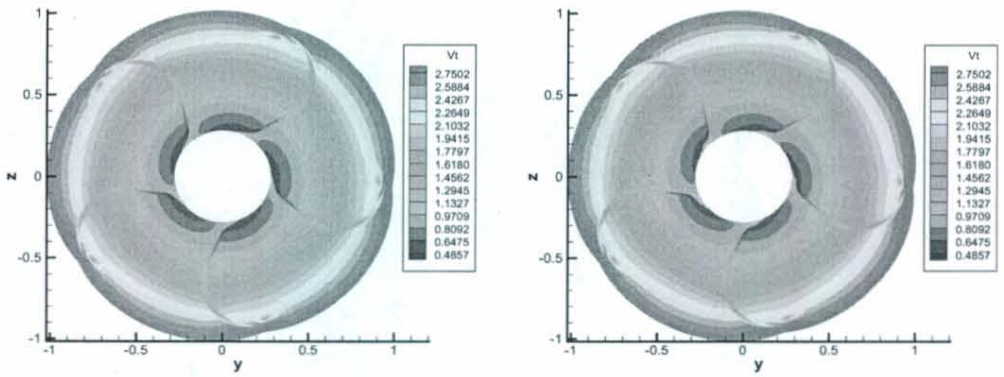

(b) $k - \epsilon$ model

(c) BSL RSM model

Figure 5-8: Tangential velocity V_t at $x/R = 0.2386$

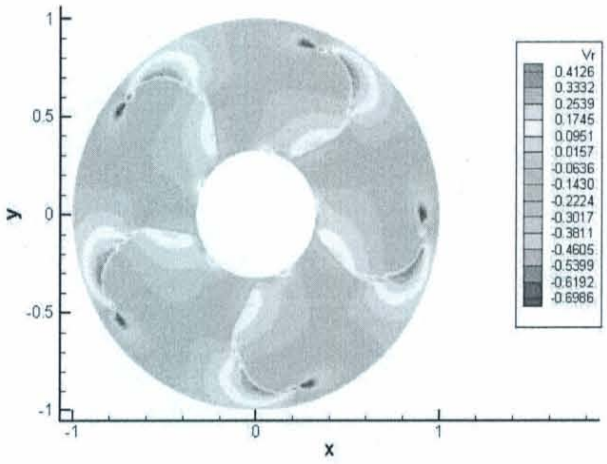

(a) Experimental results by Chesnakas and Jessup (1998)

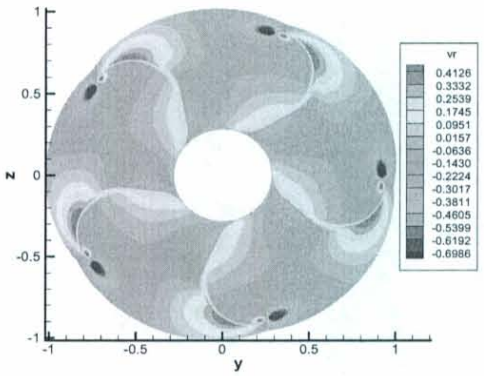

(b) $k - \epsilon$ model

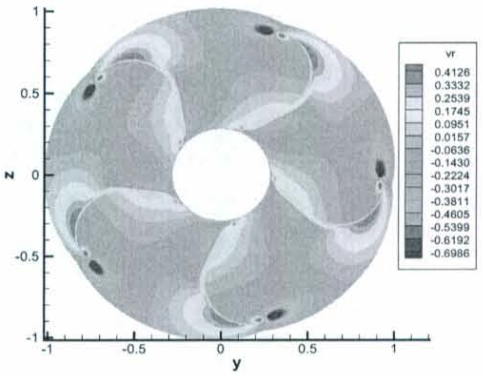

(c) BSL RSM model

Figure 5-9: Radial velocity V_r at $x/R = 0.2386$

Blade Surface Pressure

The post processor of the program *PropGGM* was modified to compute the surface pressure of the blades. The contour of surface pressure coefficient of pressure side and suction side based on the $k-\epsilon$ model and the BSL Reynolds stress model were compared with the numerical results of Hsiao and Pauley (1999) in Figures 5-10 and 5-11. In the work of Hsiao and Pauley (1999), the general characteristics of the propeller flow including the blade-to-blade flow, wake, and tip vortex were well predicted. It can be seen from the figures that both the turbulence models give similar results. Pressure side contour plot agrees well with the work of Hsiao while the suction side plot is not good enough. However, no experimental results were found to compare the pressure distributions.

Propeller Performance Analysis

The performance of marine propeller is usually determined by the thrust and torque. The numerical thrust coefficient, K_t, and torque coefficient, K_q were also computed. It was found that the numerical values underpredict the experimental K_t and K_q. A series of investigations was conducted to reveal the reason. They are described in the following sections.

(a) Numerical results by Hsiao and Pauley (1999)

(b) $k - \epsilon$ model

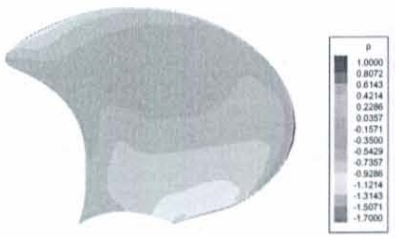

(c) BSL RSM model

Figure 5-10: Surface pressure coefficient on the pressure side

(a) Numerical results by Hsiao and Pauley (1999)

(b) $k - \epsilon$ model

(c) BSL RSM model

Figure 5-11: Surface pressure coefficient on the suction side

5.1.4 Effect of Boundary Condition

ANSYS CFX seeks pressure based boundary condition while the previous simulation had no such boundary condition. The free stream boundary condition was applied to the inlet while the outlet was set to mass flow rate, which overdefines the flow field. A test was performed by setting the outlet boundary condition to zero static pressure instead of the mass flow rate boundary. Figure 5-12 shows the comparison. In this test, $K - \epsilon$ turbulence model was employed. It is found from the figure that the mass flow rate boundary condition predicts V_r and V_x well. On the other hand, V_t is better predicted by pressure based boundary condition. K_t and K_q values for the two cases are almost same. From the observation, it can be concluded that the effect of boundary condition is negligible.

5.1.5 Effect of Timestep Size

Investigations showed that the pressure and velocity did not converge at the same time, which indicates the pressure-velocity coupling was decoupled for some reason. Though the velocities were converged in an ordinary fashion, calculation showed that propeller thrust and torque diverged with time. Figure 5-13 shows the effect.

The reason of this divergence was the choice of auto timestep size in ANSYS CFX. Any simulation which requires more then 300 iterations, an appropriate selection of timestep size is necessary to achieve good convergence (CFX manual, 2005). It provides sufficient relaxation of the equation non-linearities to obtain converged steady state solution. Too large timestep produces oscillating convergence behaviour and too small timestep slows down the convergence significantly. A judicious selection of timestep is thus important. If the timestep size is unknown, the auto timestep size of CFX can be used instead of physical timestep, but sometimes it would take forever to achieve good convergence. For most steady state problems, usually it requires fifty to hundred timesteps to achieve convergence (CFX manual,

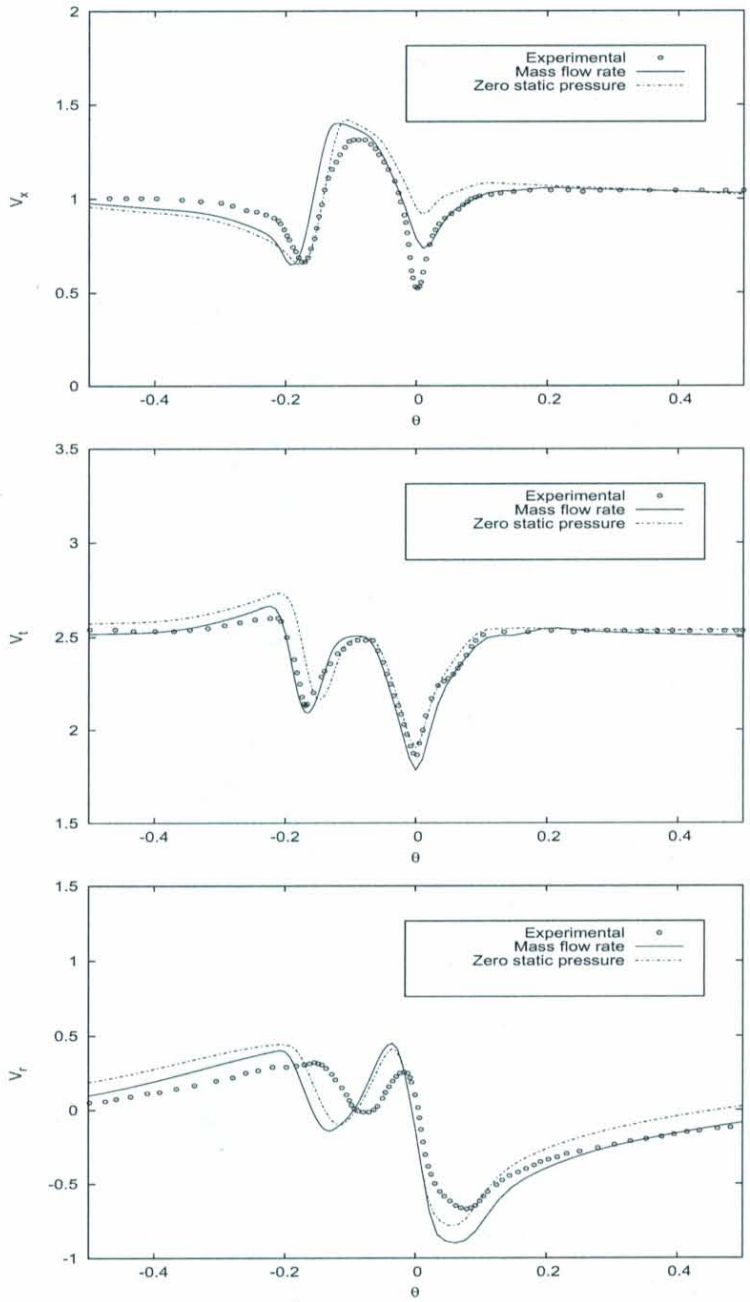

Figure 5-12: Effect of boundary conditions on Vx, Vt, Vr across the tip vortex center at $x/R = 0.2386$

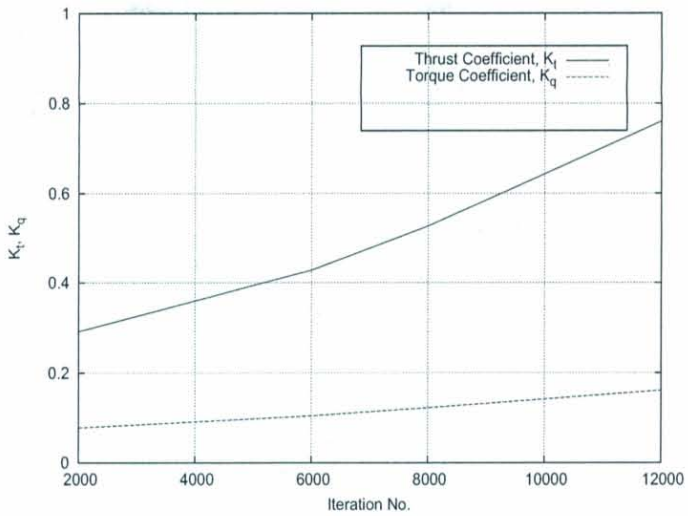

Figure 5-13: Convergence plot of K_t and K_q with auto timestep

2005). If any simulation requires more timesteps to reach a steady state solution, the smaller timestep must be used. For rotating domain, the rule of thumb to select timestep size is $1/omega$, where omega is the angular velocity. Chosen timestep size was then applied and satisfactory convergences were found. Figure 5-14 shows the convergence plot.

The new numerical values of K_t and K_q were found reasonably close to the experimental value. Table 5.3 shows the comparison. But, the computed velocity components at the tip region were not as good. The reason might be the inappropriate size of the domain. A recirculation zone was identified in the domain, which causes back flow in the domain. To stop this back flow, the outlet should be moved further. Further investigations with larger domain are required to come to a meaningful conclusions.

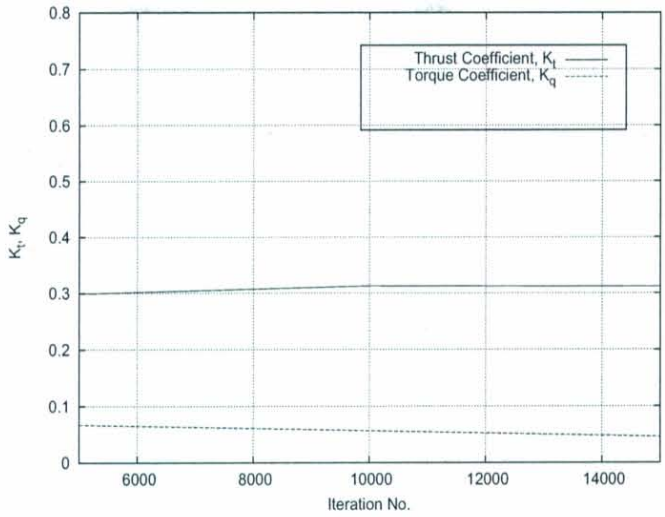

Figure 5-14: Convergence plot of K_t and K_q with physical timestep

Table 5.3: Comparison of K_t and K_q

Variables	Comp.	Exp.	Error
K_t	0.312	0.313	0.32%
K_q	0.0669	0.0783	15%

5.2 Unsteady Case

The numerical simulation was also conducted to predict the flow around a propeller operating with a shaft inclination of 7.5°. The computational domain with structured grids was generated. The periodic loadings on the face and back of the blade surface were computed and validated with the experimental data.

5.2.1 Mesh Generation

The validation studies were carried out for the DTMB 4718 propeller model at the design advance coefficient, $J = 0.751$. DTMB 4718 is a three bladed propeller with moderate skew and rake. The blade sections are based on the DTMB modifications

to the NACA 66 airfoil as defined by Brockett (Brockett, 1966). A modification was made to the blade section geometry. The blunt trailing edge was replaced by a sharp edge by changing the edge thickness to zero. This was done for the simplification of the blade geometry. The modified section geometry is given in Table A.2.

The geometry of the propeller was also modified at the tip region. The chord length was set to zero. The modified geometry is given in Table A.1. The propeller model geometry and operational conditions are given in Table 5.4. In the computation, the water density and viscosity were set to $\rho_{water} = 997kg/m^3$ and $\mu_{water} = 8.89 \times 10^{-4}kgm^{-1}s^{-1}$, respectively.

Table 5.4: Principal Characteristics of DTMB 4718

Designation	Values
D, Diameter $(inch)$	24.00
Rotation	Right Hand
Number of Blades	3
Hub-Diameter Ratio	0.3
V, Advance velocity $(inch/s)$	142.1256
J, Design Advance coefficient	0.751
n, Rotation speed (RPS)	7.88

Computational Domain

The propeller model DTMB 4718 is a large diameter model (24 inches), which requires more grid cells then DTMB 5168 (15.856 inches diameter) to achieve an acceptable quality of grid. But the grid generation program *PropGGM* is limited to generate certain number of grids. On the other hand, more grids would claim more computing time. To resolve this problem, the model propeller was scaled down to half. The new characteristics of the scaled propeller were calculated following the Reynold's similitude. Table 5.5 shows the new propeller model geometry and operational conditions that was used in the simulation.

Table 5.5: New Principal Characteristics of DTMB 4718

Designation	Values
D, Diameter (*inch*)	12.00
Rotation	Right Hand
Number of Blades	3
V, Advance velocity ($inch/s$)	284.251
J, Design Advance coefficient	0.75151
n, Rotation speed (RPS)	31.52

More than 5.7 million grids were employed in the domain. Figure 5-15 shows the grid distribution over the blade surface. The spanwise and chordwise panel distribution factor (Regions 1& 2), α, was set to 0.68, spanwise stretch factor, β_1, for Region 1 was 1.05 while for Region 2, β_2, was 1.13. The chordwise stretch factors were 1.48 and 1.68 for Region 1 and Region 2, respectively .

Like the steady state domain, a spiral like single blade-to-blade computational domain was created first by setting the inlet boundary at one propeller radius upstream and the outlet boundary one diameter downstream. The outer boundary in the radial direction was located at one propeller diameter. The remaining blades and the hub were generated by simply copying and rotating the single blade domain. Figure 5-16 shows the domain. The inlet is open in the figure. Figure 5-17 shows the grids used in the computation. Following the above mentioned procedure, a single domain was created and the entire domain was set to RFR (Rotating Frame of Reference) to set its rotating speed as propeller's rotating speed. So there is no need for a stationary component and thus a GGI (General Grid Interface) interface can be ignored. Note that each GGI connection costs 5% more CPU time and memory and introduces numerical inaccuracy compared to the equivalent computation that does not use any GGI connections (CFX manual, 2005). The right-hand rule was used to determine the direction of the rotation.

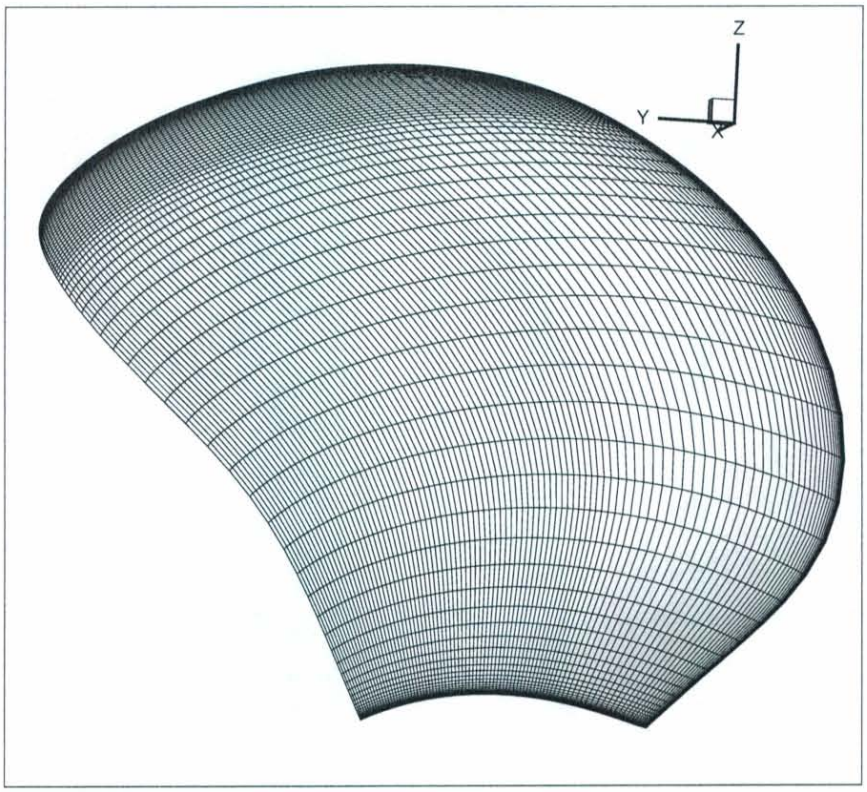

Figure 5-15: Blade surface of DTMB 4718

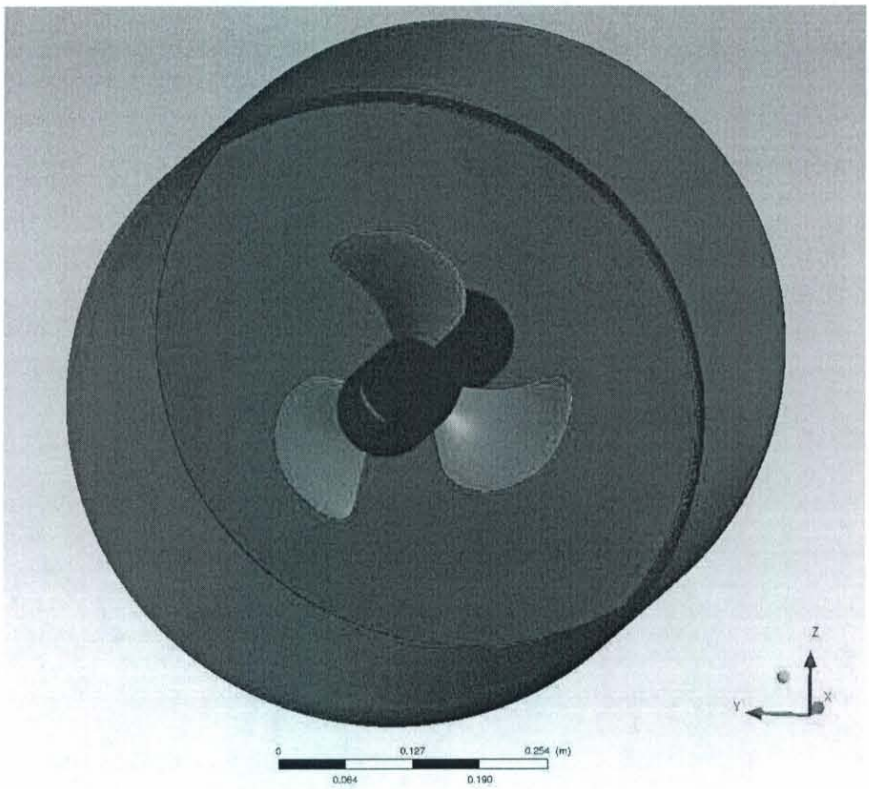

Figure 5-16: Computational domain of DTMB 4718

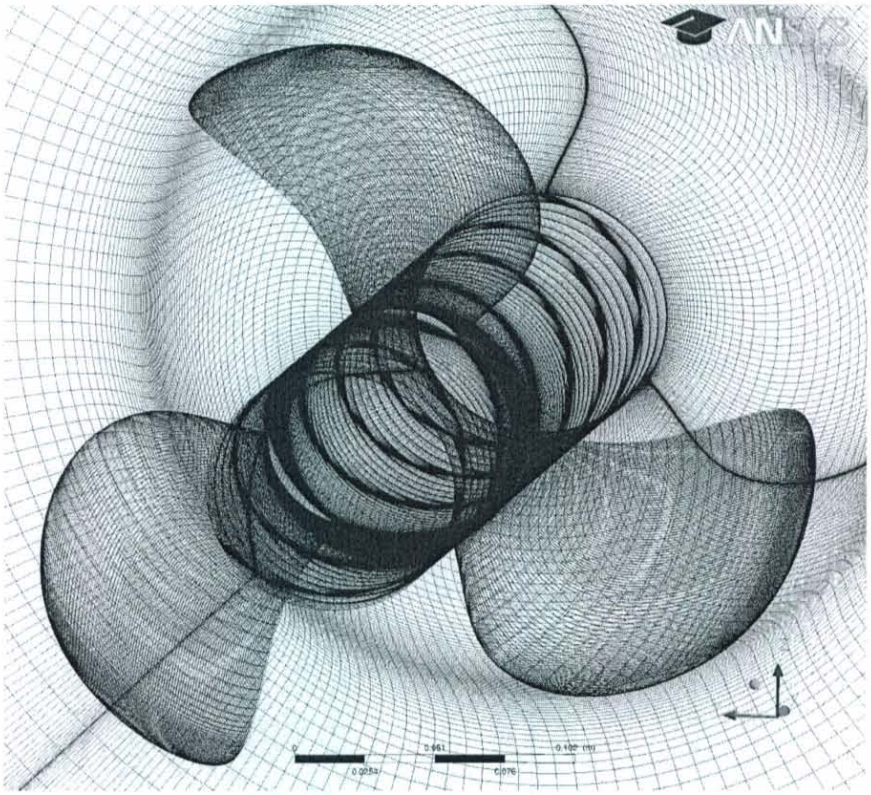

Figure 5-17: Computational grids of DTMB 4718

5.2.2 Validation of the Unsteady Domain

To validate the unsteady computational domain, a test was performed . An unsteady domain for DTMB 5168 was created first. The velocity components, V_x, V_t and V_r at the key blade were computed by using the unsteady domain. The data was then compared with the steady domain data as shown in Figure 5-18. From the figure, it is observed that V_t and V_r are in good agreement with each other. The axial velocity, V_x, at the tip region is higher than the steady domain, which is likely due to the flow interruptions among the blades. In general, it can be said that the unsteady domain is good enough for further investigation.

5.2.3 Grid Quality

The non-dimensional first grid spacing on the blade was 2×10^{-5} and was non-dimensionalized by the characteristic length which is $L_{0.7R}$. The resulting y^+ values varied between 1 and 95 over the blades. The y^+ values were also same for over the hub with peak values near the blade roots (figure 5-19). The definition for the y^+ is given by

$$y^+ = \frac{s^*}{\nu^*}\sqrt{\frac{\tau^*}{\rho^*}} \tag{5.2}$$

where, s^* is the first grid spacing. The superscript $*$ refers to dimensional variables.

5.2.4 Boundary Conditions

The boundary conditions were specified as follows. A no-slip wall condition was applied on the blades (denoted by red in the Figure 5-16) and the hub surfaces (denoted by black in the figure). A free stream inclined condition was applied on the inlet boundary (removed in the figure) and the outer surface (denoted by blue in the figure). Average static pressure was set to zero at the outlet boundary (denoted by green in the figure). Note that in steady case a comparative study of specified flow

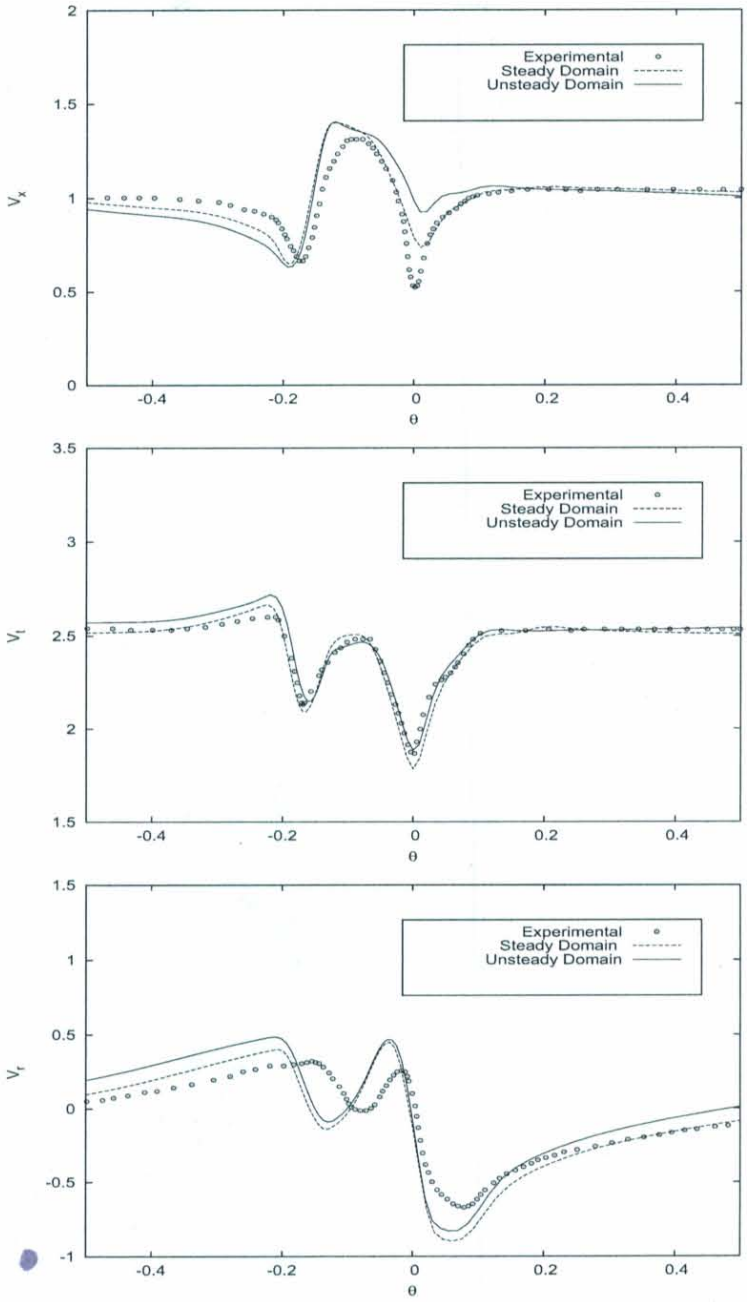

Figure 5-18: Verification of unsteady domain on Vx, Vt, Vr across the tip vortex center at $x/R = 0.2386$

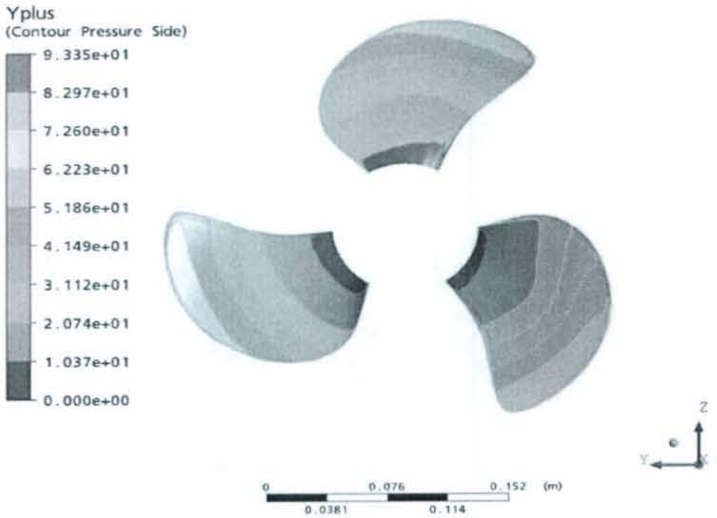

Figure 5-19: y^+ distribution over the blade surface (pressure side) on DTMB 4718

rate boundary condition and pressure based boundary condition was discussed. It was found that there is no significant difference between these two boundary conditions. Since the ANSYS CFX prefers pressure based outlet boundary condition, average static pressure was employed in this simulation instead of specified flow rate boundary condition.

5.2.5 Unsteady Simulation Technique

Initial Condition

For transient cases, initial conditions are required in the entire domain for all times $t > 0$. The solutions move forward in time and diffuse in space. The occurrence of dissipative effects ensures that the solutions are independent of initial conditions (Versteeg and Malalasekera, 1995). To achieve a good convergence and solution robustness, a transient run can be started with results from a converged steady-state

simulation, especially if it is difficult to provide an accurate estimate of the initial conditions (CFX manual, 2005). In this simulation, the unsteady simulation was performed in two steps. The steady simulation with no inclination was conducted first with 1000 iterations. This simulation data was then used as the initial conditions for the unsteady simulation.

Simulation Set-up

In the unsteady simulation, the shaft inclination causes non-uniform inflow to the propeller. To represent this cross flow condition, several techniques were implemented and none of them were found to be successful. The 7.5° inclination of the shaft produces a first harmonic variation in two of the three components of propeller inflow. The definition of this non-uniform inflow is provided by ITTC (ITTC report, 1999), and was implemented in the simulation. Another definition of two component inflow velocity in Cartesian coordinate system was also examined. Both the definitions overpredict the solution field. A new technique was then employed in this simulation. The whole computational domain was inclined following the shaft inclination angle. A new Cartesian coordinate system along with the global coordinate system was created. This new inclined coordinate was aligned with the shaft as shown in Figure 5-21. The normal inflow velocity and all other boundary conditions were set at global coordinate. Only the rotation of the propeller and its associated domain were set with respect to the inclined axis. This technique represents the real flow condition very well.

Convergence Criteria

The propeller was rotated through a sequence of discrete angular intervals and the procedure was continued through several revolutions of the propeller until steady state oscillations of the blade loading were achieved. Initially the simulation was carried out for four complete rotations of the propeller using a time step equivalent

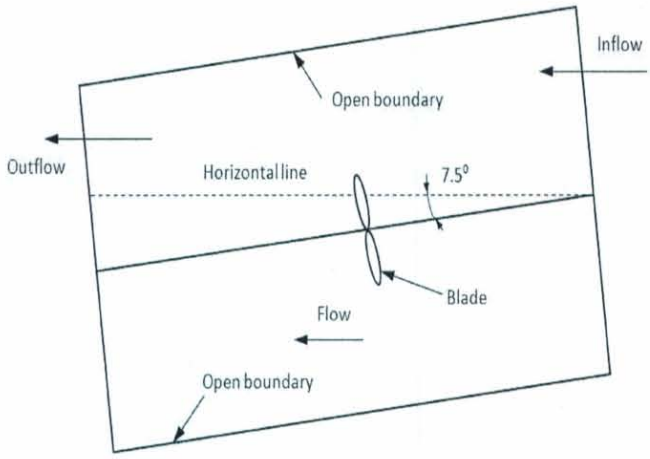

Figure 5-20: Schematic diagram of unsteady simulation set-up

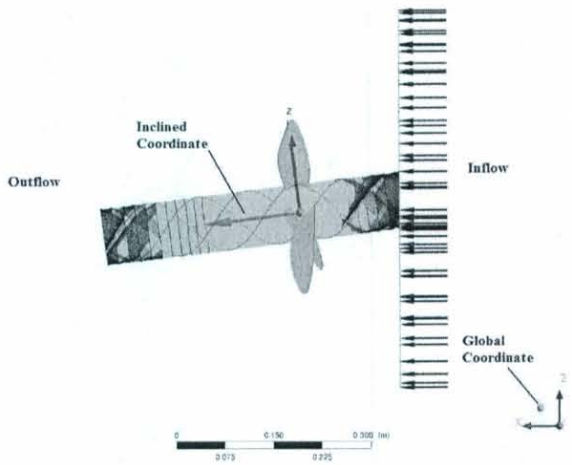

Figure 5-21: Coordinates of the unsteady simulation set-up

to a three degree rotation; a total of 480 time steps. But the solution did not converge sufficiently within the maximum number of time steps, which indicates that the CFX solver needs more iterations to achieve better convergence. A time step equivalent to a one degree rotation and a complete one second of simulation was then performed. The time step was fixed during the simulation. Note that an accurate resolution of gradients in the inflow can be achieved with such a small time step. It also reduces the number of iterations needed for the implicit solver to converge at each time step (Krasilnikov et al., 2009). The maximum number of iterations per time step was set to 10 and the RMS residuals were set to 1×10^{-4}.

Solution Strategy

Advection terms were discretised by the high resolution scheme while the viscous terms were treated by employing central difference scheme. The transient terms were descretised with Second Order Backward Euler scheme. An algebraic Multi-grid (MG) model was used to accelerate the convergence. The blended $k - \omega$ Shear Stress Turbulence model was employed in the computation. The advantage of this model is that it predicts the flow separation accurately. It has the ability to cope simultaneously with the low Re regions and high Re regions (Krasilnikov et al., 2009). The model also can predict accurately the non-equilibrium regions in the boundary layer.

Computing Resources

Huge computing resources and time were required by this simulation. At the beginning of this numerical experiment, a cluster CPU with 20 processors were used. It took $3 - 4$ weeks to complete a 0.12 second of simulation and couple of months to reach a steady state solution. Later on, the experiment was speed up by employing 104 cluster processors and the required time was reduced to $3 - 4$ days to achieve a steady state solution.

5.2.6 Convergence Tests

Several convergence tests were completed to get the right number and quality of parameters. First, a convergence test was done with the grid size of the domain. Two grid size, large and small, were compared as shown in Figure 5-22. From Figure 5-22, it was observed that the smaller grid agrees better with the data. Next, the effect of domain size was checked. A larger domain was created with around 11.5 million grids by moving the outer boundary in the radial direction to 1.5 propeller diameter and the outlet boundary to 1.5 diameter downstream. The inlet boundary stays at the same position. The effect is shown in Figure 5-23 and it shows that the domain size has no significant effect. Note that the same type of grid as in steady case, Grid I, was employed in all the tests. The test data were compared with the steady state data at $0.5R$.

Previous experience on steady simulation of DTMB 5168 shows that the default mass and momentum variables of ANSYS CFX are not often enough to monitor the convergence of a simulation. Two additional variables, K_t and C_p were created to confirm the convergence of the solution. Here, K_t is the propeller thrust coefficient and C_p is the pressure coefficient. Figure 5-24 shows the convergence of the residuals of the default variables and Figure 5-25 and 5-26 shows the convergence plots of K_t and C_p, respectively. From Figure 5-25, it is clear that the solution reached its steady state solution in about 0.5 seconds and there is no significant change in convergence after that.

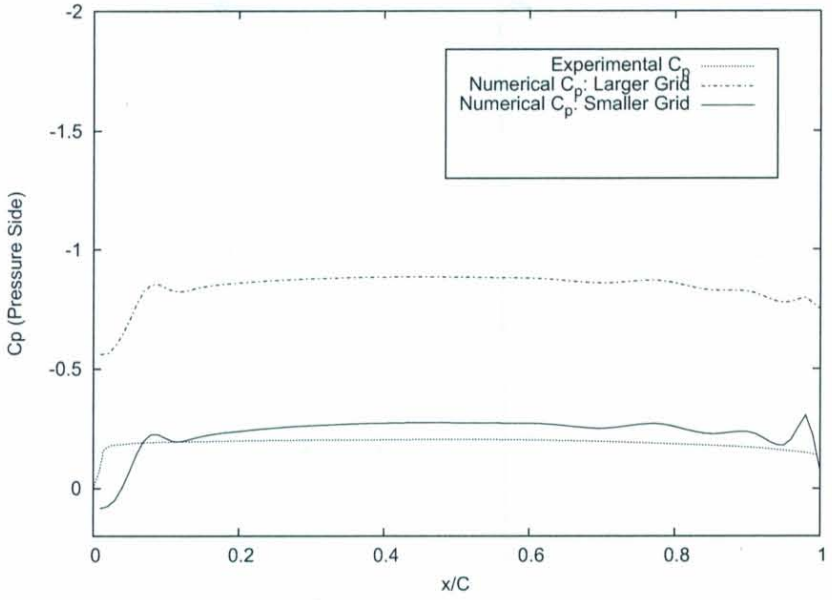

Figure 5-22: Effect of grid size on the computed C_p at $r = 0.5R$

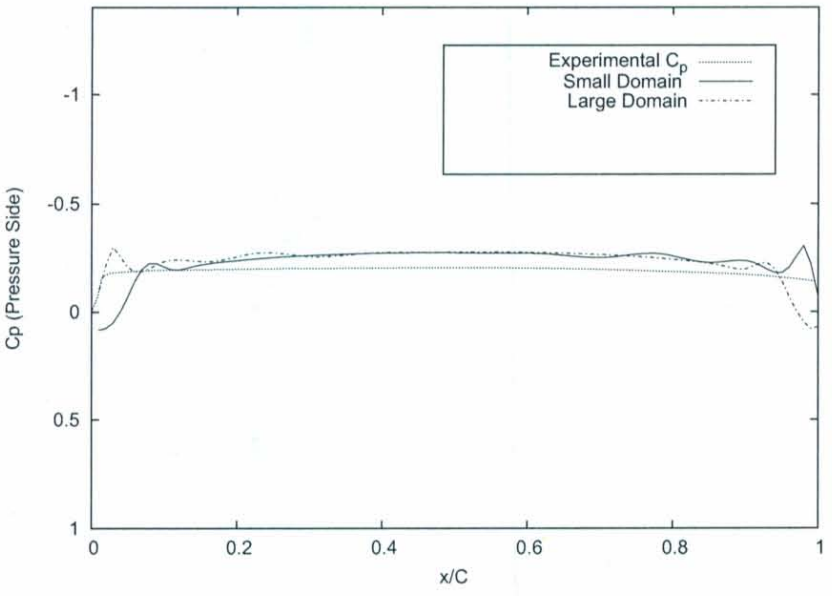

Figure 5-23: Effect of domain size on the computed C_p at $r = 0.5R$

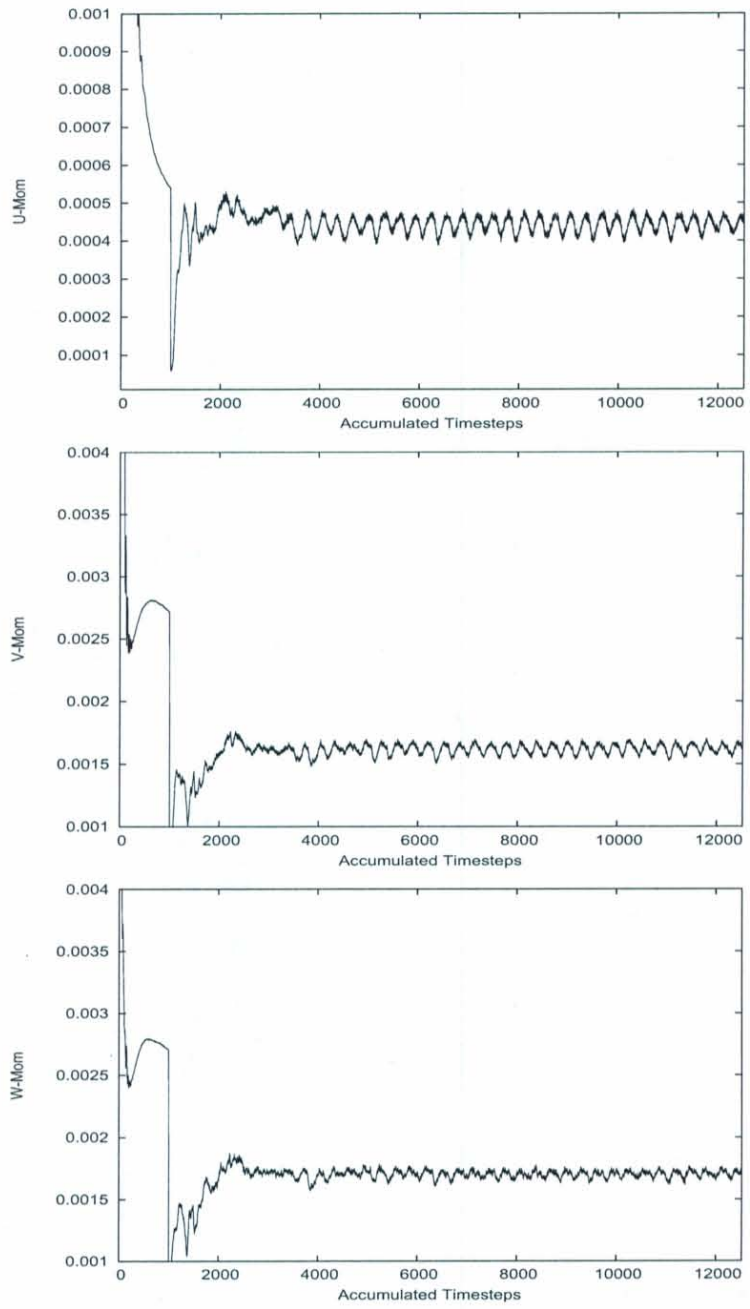

Figure 5-24: Convergence plots of mass and momentum residuals

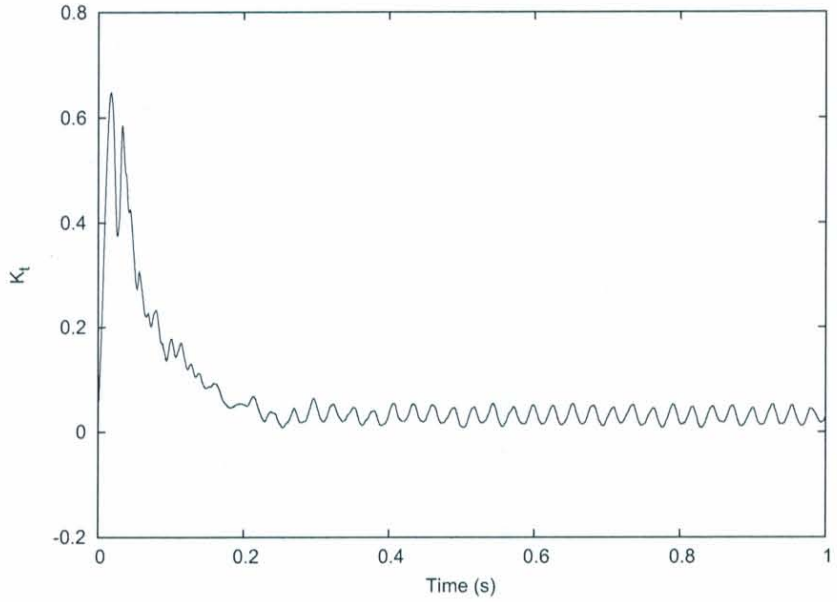

Figure 5-25: Convergence of propeller thrust coefficient with time iterations

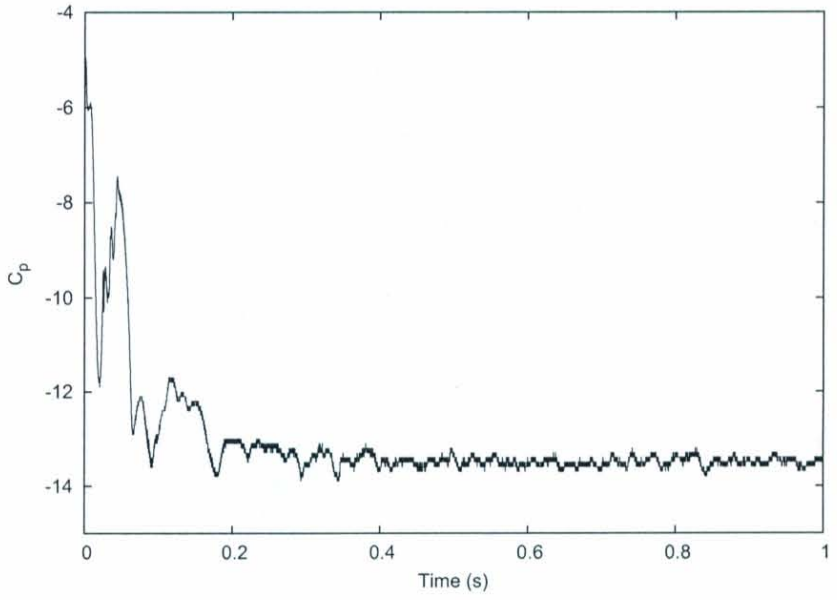

Figure 5-26: Convergence of propeller pressure coefficient with time iterations

5.2.7 Validation

The computed data was validated against the available experimental results. The time domain solution was converted to the more usual frequency domain solution by harmonic analysis of the time histories of pressure coefficients for the last complete revolution. A Fortran program was written to do this Fourier transformation. The computed pressure coefficients were compared with the experimental data and discussed in terms of the first order Fourier harmonic amplitudes and phases which are defined as:

$$C_p(t) = \overline{C_p} + C_{p1}\cos(\theta - \phi)$$

$$C_{p1} = \sqrt{a_1^2 + b_1^2}$$

$$\phi = \tan^{-1}(a_1/b_1)$$

$$a_1 = \frac{2}{T}\int_0^T C_p(t)\cos(\omega t)dt$$

$$b_1 = \frac{2}{T}\int_0^T C_p(t)\sin(\omega t)dt$$

Where, T is the total time for one complete revolution and ω is the angular velocity of propeller.

Pressure values were sampled on the key blade at points along the sections at $r = 0.5R, 0.7R$ and $0.9R$ over the last full revolution at each time step. These data were then converted by harmonic analysis to give the first harmonic amplitude, C_{p1} and phase angle, ϕ. Figures 5-27 to 5-29 compare the predicted and experimental value of amplitude and phase at $r = 0.5R, 0.7R$ and $0.9R$.

At $r = 0.5R$ (Figure 5-27), on the pressure side, the predicted amplitudes of the first harmonics are in very good agreement with the experimental data except the sudden drops near the leading edge. However, the phase prediction is less accurate. On the

suction side, the amplitude is less than the experimental data near the leading edge region and closer at the trailing edge. The phase angles are well captured at the mid chord region.

At $r = 0.7R$ (Figure 5-28), on the pressure side, the amplitude agrees with the experimental data reasonably well, though an overprediction is found at the mid chord region. On the suction side, the predicted pressure distribution has a peak at the leading edge and increases towards the trailing edge. The reason for this irregular variation along the chord could be the effect of crossflow and rollup processes of the tip vortex as explained by Jessup (1982).

At $r = 0.9R$ (Figure 5-29), on the pressure side, the computed amplitude rises at the 0.7 chord location. The modification at the tip region might be the reason. On the suction side, computed values are less than the experimental data.

Overall, it is observed that the computed results agree reasonably well with the amplitude over the pressure side at $r = 0.5R$ and $0.7R$ while the amplitude over the suction side is underpredicted. A possible explanation would be the modified tip region of the blades. According to Jessup (1982), blades with zero chord length at the tip, start the vortex at the outermost tip and the vortex travels over the suction side of the blade. The sharp leading and trailing edges could be another reason. To conform with the actual propeller geometry, ANSYS CFX seeks a blunt trailing edge, closed by an elliptical cap while a sharp trailing edge was used in the simulation due to the limitations of *PropGGM* (Leras and Hally, 2010). The differences in predictions at the two edges might be due to this simplification. Moreover, the current simulation ignored the sliding mesh approach, that is, it did not take into account the relative motion of the propeller blade inside a fixed domain, which is required for the time accurate simulation (Snchez-Caja

et al., 2008). The less favourable predictions of the phase angles are likely due to this.

The computed mean thrust, K_t, at the design condition is found 0.047 while the design K_t is 0.055. The calculated mean torque coefficient, K_q, is 0.0104 while the design K_q is 0.0106. Figure 5-30 shows the K_t variation with the angular position of the key blade. Unfortunately, no data was found to compare with the result.

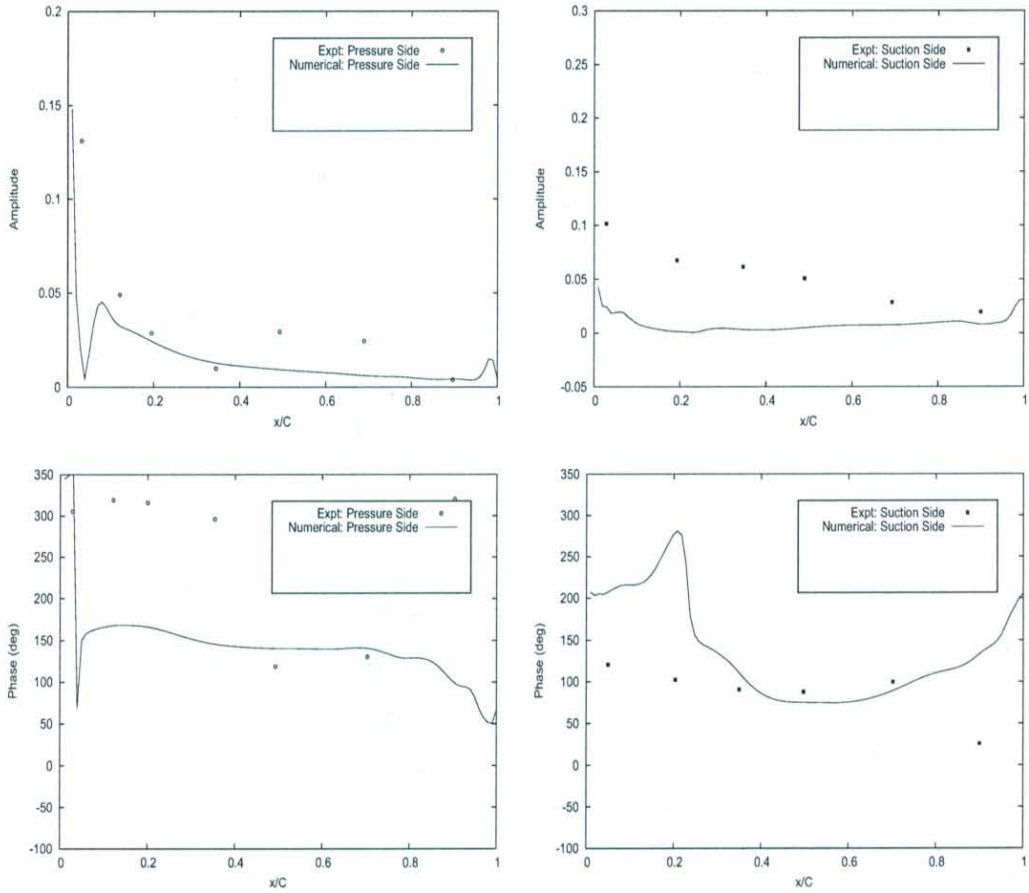

(a) Pressure side (b) Suction side

Figure 5-27: Computed first harmonic amplitude and phase of the pressure coefficient on DTMB 4718 with $J = 0.751$ at $0.5R$

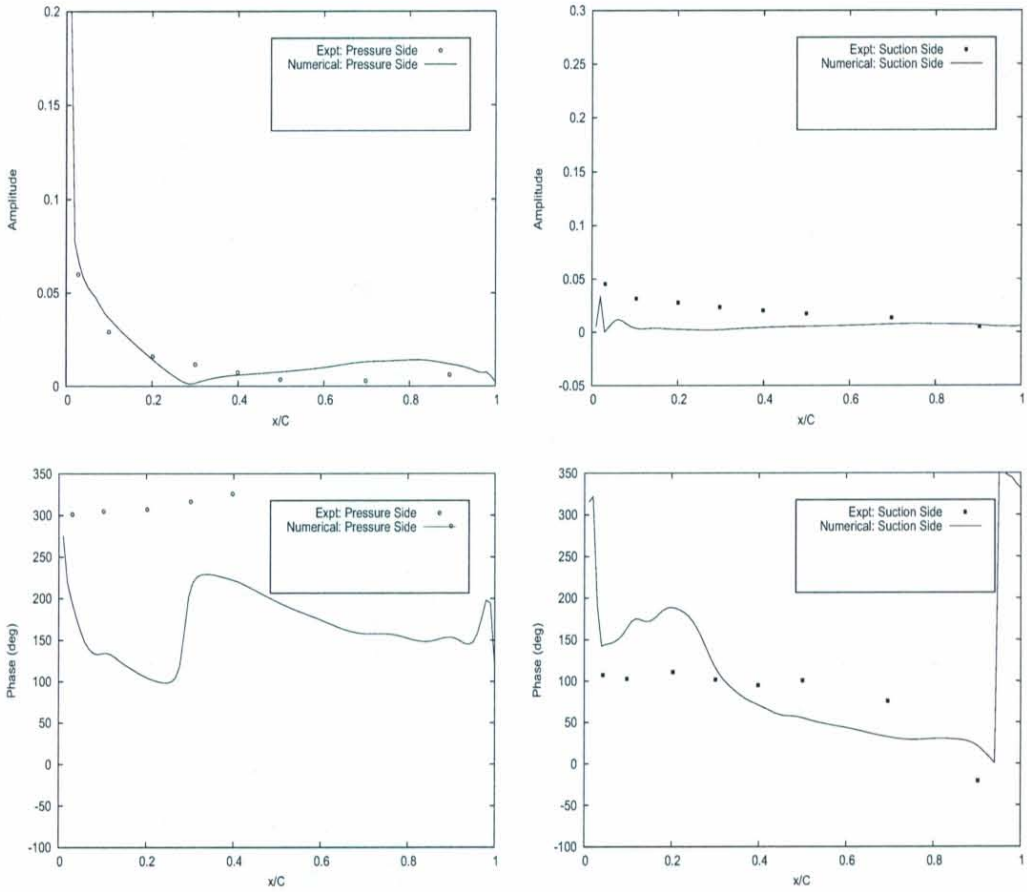

(a) Pressure side (b) Suction side

Figure 5-28: Computed first harmonic amplitude and phase of the pressure coefficient on DTMB 4718 with $J = 0.751$ at $0.7R$

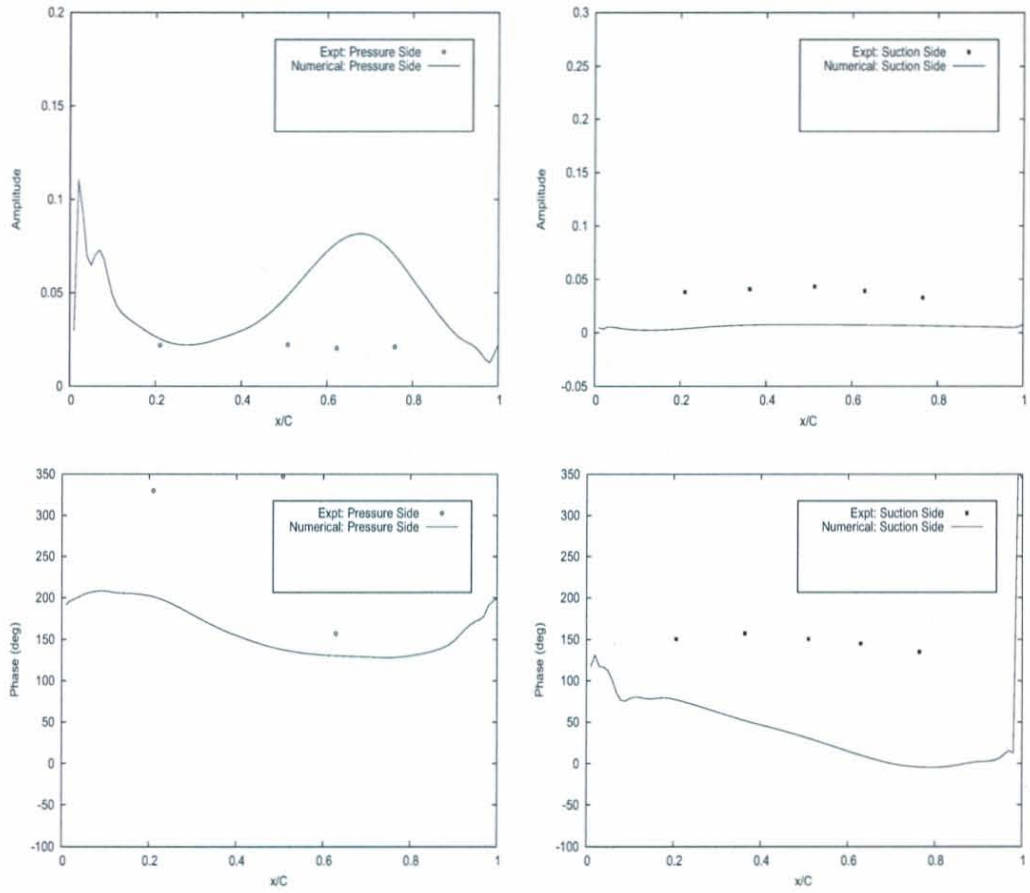

(a) Pressure side (b) Suction side

Figure 5-29: Computed first harmonic amplitude and phase of the pressure coefficient on DTMB 4718 with $J = 0.751$ at $0.9R$

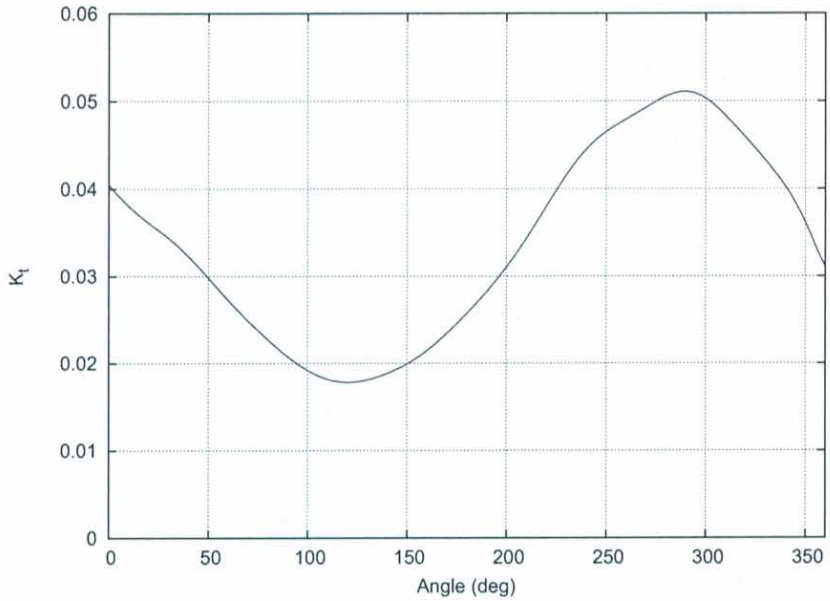

Figure 5-30: Computed thrust variation with the angular position of blade

Chapter 6

Conclusions and Recommendations

6.1 Steady Case

The effect of turbulence modeling on propeller tip vortex computation was investigated using the RANS solver ANSYS CFX. The grid generation program *PropGGM* was used to generate a spiral-like structured grid with grid concentration at the vortex core.

Validation studies were carried out for the DTMB 5168 model propeller at open water condition. The post processor of the program *PropGGM* was modified to give the non-dimensional velocities and the surface pressure of the blades. Various eddy viscosity turbulence models and Reynolds stress models were employed in the computations. Both the eddy viscosity turbulence models and the Reynolds stress models gave almost similar predictions of the vortex flow. There was no indication found that the Reynolds stress models significantly improve the vortex flow prediction in the near field. It was shown that the two-equation and the Reynolds stress models are considered slightly better than the zero-equation and one-equation turbulence models for the vortex flow computation.

Pressure distributions over the blade surfaces were computed and compared with other numerical results. Reasonably good agreements were observed for the pressure distributions on the pressure side. The suction side pressure distributions were less favourable.

Despite the success of tip vortex computation, the current investigation underpredicts the thrust and torque coefficient of the propeller. Several investigations were performed and found the significant effect of auto timestep size on the simulation. The simulation technique was improved by introducing physical timestep and a better prediction of thrust and torque coefficient was achieved. However, the velocity components were not in a good agreement. A back flow in the domain was identified and it was concluded that the smaller domain size could be the reason.

6.2 Unsteady Case

In the second part of this research, the unsteady simulation of the propeller flow was conducted using the same RANS solver ANSYS CFX. Considering the limitations of *PropGGM*, a computational domain with structured grid was generated. A program was developed to generate the surface coordinates of the blade by taking the basic propeller geometry. Convergence studies were done to select the best and least number of grids. A simulation technique for inclined flow was presented.

Validation studies were carried out for the DTMB 4718 model propeller at design condition. A program for the harmonic analysis of the time domain solution was developed. The results obtained are encouraging. It was demonstrated that the current simulation reasonably predict the amplitude of the pressure variations on the pressure side. The prediction of the pressure variations on the suction side is less favourable, which could be caused by the modification of the blade geometry. The

relative motion of the propeller blade was not captured in the simulation, which might be another reason .

6.3 Future Work

This section outlines some suggestions to improve the propeller flow simulation. The future works for the numerical simulation of propeller flow are suggested to include the following:

- The grid generation program *PropGGM* has to be improved. For highly skewed and raked propellers, a manual modification of the geometry is required to generate smooth blade-to-blade boundaries. This modification changes the propeller geometry and may not be acceptable for tip vortex assessment. The process should be automated.

- For the steady simulation of tip vortex computation, the next logical step appears to examining the effect of domain size. The outlet should be moved further; at least 6 diameters of the propeller to protect the back flow in the region.

- For the inclined flow case, the work can be extended to the computation of propeller flow at off design conditions.

- The large computing time is a big hindrance for this numerical simulation. A simple unsteady simulation takes couple of months to converge in a super computer of 20 processors. Concentration also should be given to find out the alternative simulation technique to reduce the computing time.

Bibliography

Abdel-Maksoud, M. and Heinke, H.J., 2002, "Scale Effects on Ducted Propellers", *Proceedings of 24th Symposium on Naval Hydrodynamics*, Fukuoka, Japan.

Abdel-Maksoud, M., Hellwig, K., and Blaurock, J., 2004, "Numerical and Experimental Investigation of the Hub Vortex Flow of a Marine Propeller", *Proceedings of 25th Symposium on Naval Hydrodynamics*, St. John's, Canada.

Billet, M.L., 1987, "Wake Measurements Using a Laser Doppler velocimeter System", *ITTC Symposium on Appliaction and Accuracy of LDV Measurements*

Boswell, R., Jessup, S., and Kim, K.-H., 1981, "Periodic Single-blade Loads on Propellers in Tangential and Longitudinal Wakes", *SNAME Propellers '81 Symposium*, Virginia Beach, VA, USA, May 26-27.

Boswell, R., Jessup, S., Kim, K.-H., and Dahmer, D., 1984, "Single-blade Loads on Propellers in Inclined and Axial Flows",*Technical report, DTNSRDC-84/084,DTNSRDC, November.*

Boswell, R.J., Nelka, J.J, and Denny, S.B., 1976, "Experimental Determination of Mean and Unsteady Loads on a Model CP Propeller Blade for Various Simulated Modes of Ship Operation", *The Eleventh Symposium on Naval Hydrodynamics, pp. 789-823 and 832-834*, London and New York

Boswell, R.J., Nelka, J.J, and Denny, S.B., 1978, "Experimental Unsteady and Time-Average Loads on the Blades of a CP Propeller Behind a Model of the DD-963

Class Destroyer", *Propellers '78 Symposium, The Society of Naval Architects and Marine Engineers*, Virginia Beach, Virginia

Brockett, T., 1966 "Minimum Pressur Envelopes for Modified NACA-66 Sections with NACA a=0.8 Camber and BuShips Type I and Type II Sections" *(Report 1780) David W. Taylor Naval Ship Research and Development Center.*

Carlton, J. S., 1994 Marine Propellers and Propulsion, Second Edition, *Oxford; Boston : Butterworth-Heinemann*

Cendese, A., 1985, "Phase Sampling inthe Analysis of a Propeller Wake", *International Conference on Laser Anemometry-Advances and Application*, Manchester, U.K.

CFX Manual, 2005, Version 10.0

Chen, B. and Stern, F., 1998, "RANS Simulation of Marine-Propulsor P4119 at Design Condition", *Proceedings of 22nd ITTC Propulsion Committee Propeller RANS/PANEL Method Workshop*, Grenoble, France.

Chesnakas, C.J. and Jessup, S.D., 1998, "Propeller Tip Vortex Measurements Using 3-Component LDV", *Proceedings of 22nd Symposium on Naval Hydrodynamics*, Washington D.C., U.S.A.

Di Felice, F., Di Florio, D., Felli, M., and Romano, G.P., 2004, "Experimental Investigation of the Propeller Wake at Different Loading Conditions by Particle Image Velocimetry", *Journal of Ship Research, Vol.48, No. 2.*

Gaggero S., 2010, "Development of a Potential Panel Method for the Analysis of Propellers Performances in Cavitating and Supercavitating Conditions", *Ph.D. Thesis*, University of Genoa, Italy

Gaggero, S., Villa, D. and Brizzolara, S., 2010, "RANS and PANEL Method for Unsteady Flow Propeller Analysis", *9th International Conference on Hydrodynamics, October 11-15, 2010 Shanghai, China*

Hess, J.L. and Valarezo, W.O., 1985, "Calculation of Steady Flow about Propellers by Means of Surface Panel Method." *Proceedings, Research and Technology Douglas Aircraft Company, Long Beach,CA.*

Hsiao, C. T. and Pauley, L.L., 1999, "Numerical Computation of the Tip Vortex Flow Generated by a Marine Propeller", *ASME Journal of Fluids Engineering, Vol. 121, No. 3.*

Hsin C Y, 1990, "Development and Analysis of Panel Methods for Propeller in Unsteady Flow", *Ph.D. Thesis*, Massachusetts Institute of Technology, USA

"ITTC Report of the Propulsion Committee" 22^{nd} *ITTC Proceedings*

Jessup, S.D., 1982, "Measurement of the Pressure Distribution on Two Model Propellers", *(Report DTNSRDC-82/035) David W. Taylor Naval Ship Research and Development Center*, Bethesda, Maryland.

Jessup, S.D., 1989, "An Experimental Investigation of Viscous Aspects of Propeller Blade Flow." *PhD thesis*, The Catholic University of America.

Jessup, S.D., 1990, "Measurement of Multiple Blade Rate Unsteady Propeller Forces", *Technical report, DTRC-90/015, May.*

Jessup, S.D., 1994, "Propeller Blade Flow Measurements Using LDV", *ASME Summer Fluids Division Meeting*, Lake Tahoe, NV.

Jessup, S.D., Boswell, R.J., and Kim, K.-H., 1977, "Experimental Unsteady and Time-Average Loads on the Blades of the CP Propeller on a Model of the DD-963 Class Destroyer for Simulated Modes of Operation", *DTNSRDC Report 77-0110*

Kerwin, J. and Lee, C. S., 1978, "Prediction of Steady and Unsteady Marine Propeller Performance by Numerical Lifting Surface Theory" *Transactions of Society of Naval Architects and Marine Engineers*

Kerwin, J.E., Kinnas, Spyros, A., Lee, Jin-Tae, Shih and Wei-Zen, 1987, "A Surface Panel Method for the Hydrodynamic Analysis of Ducted Propellers." *Transactions of Society of Naval Architects and Marine Engineers 95, pp. 93-122.*

Kinnas, S.A. and Hsin, C.Y., 1992, "Boundary Element Method for the Analysis of the Unsteady Flow Around Extreme Propeller Geometries." *AIAA Journal, Vol. 30, No. 3*

Kobayashi, S., 1981, "Experimental Methods for the Prediction of the Effect of Viscosity on Propeller Performance ", *MIT Department of Ocean Engineering, Report No. 81-7.*

Krasilnikov, V., Zhang, Z. and Hong, F., 2009, "Analysis of Unsteady Propeller Blade Forces by RANS", *First International Symposium on Marine Propulsors, Trondheim, Norway, June 2009*

Launder, B.E., Reece, G.J. and Rodi, W., 1975, "Progress in the Developments of a Reynolds-stress Turbulence Closure" *J. Fluid Mechanics, Vol. 68, pp.537-566*

Lee, C.S., 1979, "Prediction of Steady and Unsteady Performance of Marine Propellers with or withourt Cavitaion by Numerical Lifting-Surface Theory." *PhD thesis*, Massachusetts Institute of Technology, May 1979

Leras, P.E. and Hally, D., 2010, "RANS Calculations of the Flow Past Inclined Propellers" *Technical Memorandum, DRDC Atlantic TM 2009-266, May.*

Lewis, E. V. , 1988, "Principles of Naval Architecture", Vol-2, *Jersey City : Society of Naval Architects and Marine Engineers*

Liu, L., 2009, "Computation of Propeller Tip Vortex Flow" *Masters thesis*, Memorial University of Newfoundland, St. John's, Newfoundland, Canada

Liu, P. and Bose, N., 1998, "An Unsteady Panel Method for Highly Skewed Propellers in Non-uniform Inflow." *22nd ITTC Propulsion Committee Propeller RANS/Panel Method Workshop. Grenoble,France,pp.343-349.*

Menter, F.R., 1994, "Two-equation Eddy-viscosity Turbulence Models for Engineering Applications" *AIAA-Journal., 32(8)*

Menter, F.R., 1994, "Eddy Viscosity Transport Equations and their Relation to the $k-\epsilon$ Model" *NASA Technical Memorandum 108854*

Min, K.S., 1978, "Numerical and Experimental Methods for Prediction of Field Point Velocities around Propeller Blades", *MIT Department of Ocean Engineering, Report No. 78-12. 1978.*

Paterson, E.G. and Stern, F., 1997, "Computation of Unsteady Viscous Marine-Propulsor Blade Flows-Part 1: Validation and Analysis", *Journal of Fluids Engineering*, MARCH 1997, Vol. 119 pp. 145-154

Politis, G. K. 2004, "Simulation of Unsteady Motion of a Propeller in a Fluid Including Free Wake Modeling." *Engineering Analysis with Boundary Elements, Vol. 28, page 633-653.*

Qiu, W. Peng, H. and Brennan, D., 2003, "Development of Surface Geometry and External Flow field Gridding Software for the Computation of Propeller Surface and Tip Vortex Flow" *DRDC Atlantic CR2003-91*, Defence R & D Canada Atlantic, Nova Scotia, Canada.

Qiu, W., Peng, H., Liu, L., Mintu, S., Hally, D. and Hsiao, C.T., 2010, "Effect of Turbulence Modeling on RANS Computation of Propeller Tip Vortex Flow"

Proceedings of the Twentieth (2010) International Offshore and Polar Engineering Conference, Beijing, China

Raw, M.J., 1996, "Robustness of Coupled Algebraic Multigrid for the Navier-Stokes Equations" *AIAA 96-0297, 34th Aerospace and Sciences Meeting & Exhibit*

Rhee, S.H. and Joshi, S., 2003, "CFD Validation for a Marine Propeller Using a Unstructured Mesh based RANS Method", *FEDSM03*, Honolulu, USA.

Rhee, S.H. and Koutsavdis, E., 2003, "Unsteady Marine Propulsor Blade Flow -A CFD Validation with Unstructured Dynamic Meshing", *33rd AIAA Fluid Dynamics Conference*, Orlando, FL, June, 2003

Rhie, C.M. and Chow, W.L., 1982, "A Numerical Study of the Turbulent Flow Past an Isolated Airfoil with Trailing Edge Separation" *AIAA Paper 82-0998*

Snchez-Caja, A., Pylkknen, J.V. and Sipil, T. P., 2008, "Simulation of the Incompressible Viscous Flow around Ducted Propellers with Rudders Using a RANSE Solver", *27th Symposium on Naval Hydrodynamics, Seoul, Korea, 5-10 October 2008*

Simonsen, C.D. and Stern, F., 2005, "RANS Maneuvering Simulation of Esso Osaka with Rudder and a Body-Force Propeller", *Journal of Ship Research, Vol 49, No. 2.*

Speziale, C.G., Sarkar, S. and Gatski, T.B., 1991, "Modelling the Pressure-strain Correlation of Turbulence: an Invariant Dynamical Systems Approach" *J. Fluid Mechanics, Vol. 277, pp. 245-272*

Stanier, M.J., 1992, "Design and Evaluation of New Propeller Blade Sections", *International Symposium on Propulsors and Cavitation*, Hamburg, Germany.

Versteeg, H. K. and Malalasekera, W., 1995, "An Introduction to Computational Fluid Dynamics - The Finite Volume Method" *Harlow : Prentice Hall*

Wilcox, D.C., 1986, "Multiscale Model for Turbulent Flows" *AIAA 24th Aerospace Sciences Meeting. American Institute of Aeronautics and Astronautics*

Appendix A

Geometry of DTMB 4718

Table A.1: Modified Propeller Geometry of DTMB 4718

r/R	c/D	P/D	IT/D	SKEW(Degree)	T/c	F/c
0.300000	0.187000	0.718000	0.000000	-1.650000	0.249700	0.000000
0.400000	0.249000	0.796000	0.000000	-4.050000	0.177100	0.004400
0.500000	0.311000	0.855000	0.000000	-5.000000	0.128000	0.008500
0.600000	0.366000	0.886000	0.000000	-3.500000	0.091000	0.009900
0.700000	0.403000	0.888000	0.000000	0.400000	0.063000	0.010100
0.800000	0.409000	0.870000	0.000000	5.750000	0.046900	0.009700
0.900000	0.365000	0.825000	0.000000	12.400000	0.041900	0.008200
0.950000	0.311000	0.786000	0.000000	16.100000	0.041800	0.006500
1.000000	0.000000	0.734000	0.000000	20.000000	0.041400	0.009000

Table A.2: Blade Section Geometry: Brocket

Xc	t/T	f/F
0.000000	0.000000	0.000000
0.007596	0.163400	0.060060
0.030154	0.321600	0.123810
0.066967	0.477600	0.336840
0.116978	0.627000	0.498740
0.178606	0.761400	0.654070
0.250000	0.872600	0.790510
0.328990	0.952000	0.898310
0.413176	0.994400	0.969940
0.500000	0.992400	1.000000
0.586824	0.942400	0.985030
0.671010	0.849400	0.923060
0.750000	0.722400	0.812120
0.821394	0.594400	0.638840
0.883022	0.421600	0.422270
0.933013	0.280400	0.234230
0.969846	0.166000	0.099820
0.992404	0.092400	0.023650
1.000000	0.000000	0.000000

Table A.3: Blade Section Geometry, NACA 66(DTMB Mod.), a=0.8 Meanline

Xc	t/T	f/F
0.0000	0.0000	0.0000
0.0125	0.2088	0.0907
0.0250	0.2932	0.1586
0.0500	0.4132	0.2712
0.0750	0.5050	0.3657
0.1000	0.5814	0.4482
0.1500	0.7042	0.5869
0.2000	0.8000	0.6993
0.3000	0.9274	0.8635
0.4000	0.9904	0.9615
0.4500	1.0000	0.9881
0.5000	0.9924	1.0000
0.6000	0.9306	0.9786
0.7000	0.8070	0.8892
0.8000	0.6220	0.7027
0.9000	0.3754	0.3586
0.9500	0.2286	0.1713
1.0000	0.0000	0.0000

Appendix B

Additional Figures

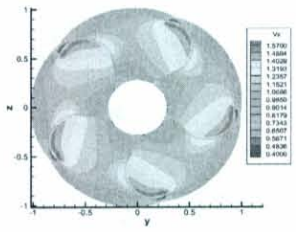

(a) Zero equation model

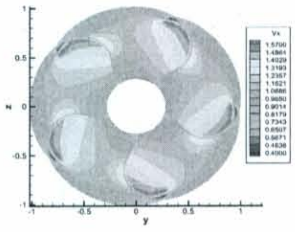

(b) $(k-\epsilon)_{1E}$ model

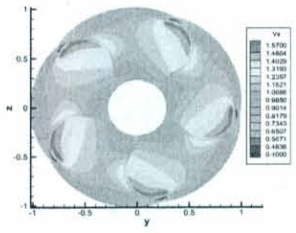

(c) RNG $k-\epsilon$ model

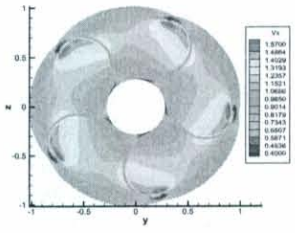

(d) SST model

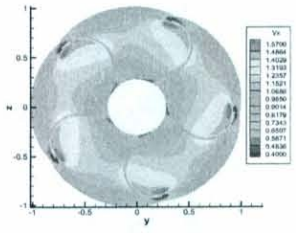

(e) SSG RSM model

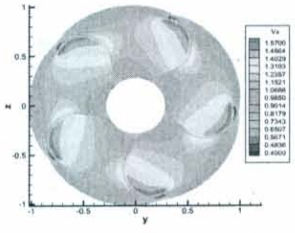

(f) LRR-IP RSM model

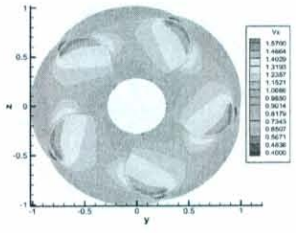

(g) LRR-QI RSM model

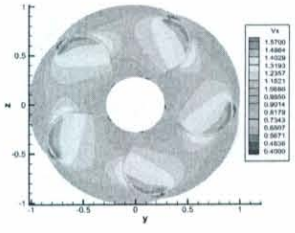

(h) Omega RSM model

Figure B-1: Additional contour plots of axial velocity V_x at $x/R = 0.2386$

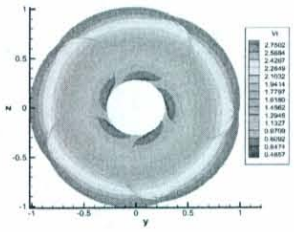

(a) Zero equation model

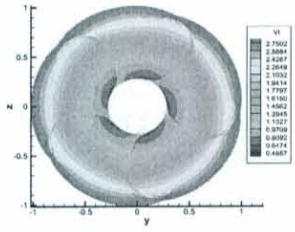

(b) $(k-\epsilon)_{1E}$ model

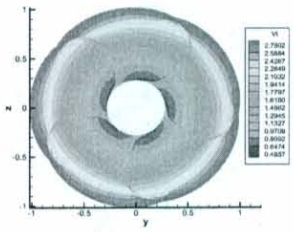

(c) RNG $k-\epsilon$ model

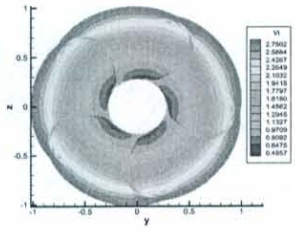

(d) SST model

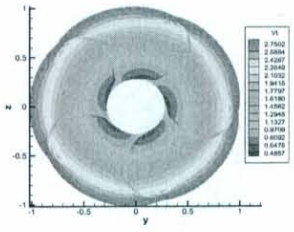

(e) SSG RSM model

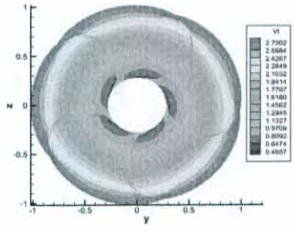

(f) LRR-IP RSM model

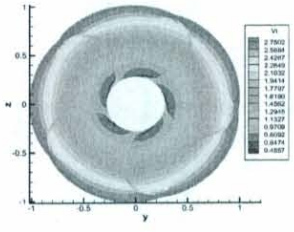

(g) LRR-QI RSM model

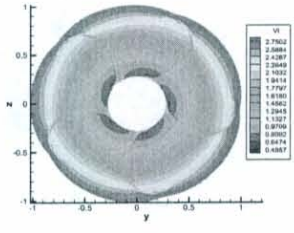

(h) Omega RSM model

Figure B-2: Additional contour plots of tangential velocity V_t at $x/R = 0.2386$

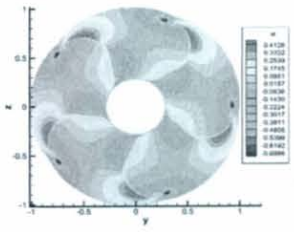

(a) Zero equation model

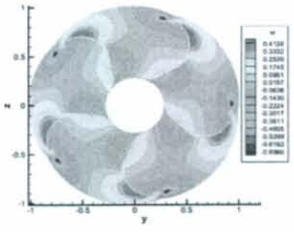

(b) $(k-\epsilon)_{1E}$ model

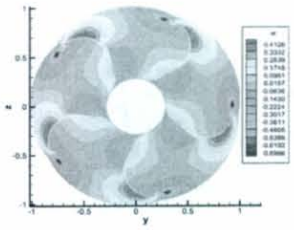

(c) RNG $k-\epsilon$ model

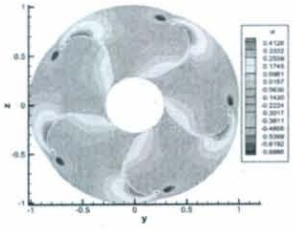

(d) SST model

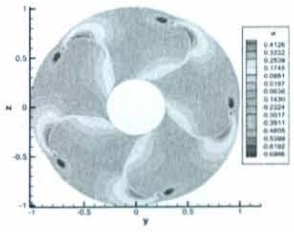

(e) SSG RSM model

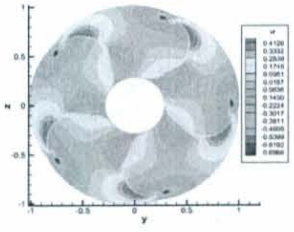

(f) LRR-IP RSM model

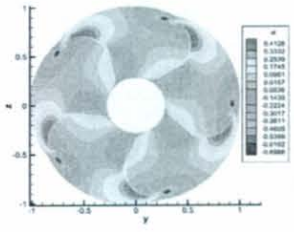

(g) LRR-QI RSM model

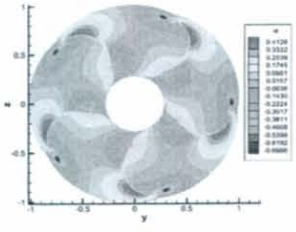

(h) Omega RSM model

Figure B-3: Additional contour plots of radial velocity V_r at $x/R = 0.2386$